International Journal of Non-Linear Mechanics 130 (2021) 103682

Contents lists available at ScienceDirect

International Journal of Non-Linear Mechanics

journal homepage: www.elsevier.com/locate/nlm

Nonlinear vibro-acoustic behavior of cylindrical shell under primary resonances

Amir Hossein Orafa, Mohammad Mahdi Jalili *, Ali Reza Fotuhi

Department of Mechanical Engineering, Yazd University, P.O. Box 89195-9741, Yazd, Iran

ARTICLE INFO

Keywords:
Cylindrical shell
Nonlinear vibration
Transmission loss
Bifurcation

ABSTRACT

Nonlinear vibro-acoustic behavior of cylindrical shell excited by an oblique incident plane sound wave under primary resonances is analytically examined in this paper. Donnell's nonlinear shallow shell theory is used to model the cylindrical shell. Coupled nonlinear differential equations of the system are analytically derived using Galerkin's approach. The Multiple Scales Method is hence, employed to solve the corresponding nonlinear equations. Then, the effects of crucial design parameters including incident sound wave amplitude, damping ratio and thickness of the shell on the characteristics of the sound transmission loss are studied for different resonance cases. In addition, the effect of detuning parameter on the bifurcation and behavior of the limit cycle under primary resonance is examined. The results show that the detuning parameter is a bifurcation parameter and Neimark–Sacker, flip, and period-3 bifurcations occur when this parameter is varied. Also, according to the results, by getting away from the resonance frequencies, excitation level incorporates no significant effect on the transmission loss of the shell.

1. Introduction

Vibro-acoustic analysis of cylindrical shells has extensively been investigated in the recent years because of their variety of engineering applications. Several cases may be addressed in aircraft, mechanical, marine and automotive engineering. Different aspects of vibro-acoustic behavior of cylindrical shell have already been addressed in the literature. Noise transmission through and radiation from the cylindrical shells were studied by many researchers. Daneshjou et al. [1] calculated the transmission loss of a homogeneous isotropic thick-walled cylindrical shell due to an oblique plane wave. Oliazadeh and Farshidianfar [2] used exact analytical approach to investigate sound transmission losses in double- and triple-walled thin cylindrical shells with varying air gap sizes. A theoretical model was developed by Zhang et al. [3] to investigate the effect of perforation on the sound transmission through a double-walled cylindrical thin shell excited by a plane wave. An analytical model based on statistical energy analysis theory was developed and experimentally validated by Oliazadeh et al. [4] to examine sound transmission through a thin-walled circular cylindrical shell. A precise transfer matrix method was developed by Wang et al. [5] to calculate the sound radiation of submerged double-walled cylindrical shell with uniformly distributed annular plates and arbitrary boundary conditions. The wave and finite element (WFE) method was developed by Kingan et al. [6] for analyzing sound transmission through, and radiation from an infinitely long cylindrical structure filled and surrounded by fluids.

Sound transmission has also been investigated through sandwich cylinders. Among these works, Magniez et al. [7] used the first-order shear deformation theory to investigate the transmission loss of an infinite multilayer cylinder composed of two orthotropic thin skins separated by an isotropic polymer core. Using the three-dimensional theory of elasticity, the acoustic wave transmission across an imperfect-bonding double-walled sandwich cylinder with FGM-core was studied by Talebitooti et al. [8].

Laminated composite cylindrical shell structures have widely been used particularly in aerospace and marine industries due to their high strength to weight ratio. Several studies have been carried out to investigate transmission loss through these structures. For example, Talebitooti et al. [9] used the Third-order Shear Deformation Theory to investigate the transmission loss of the laminated composite cylindrical shell in contrast to plane sound wave. The transmission loss of an arbitrary thick infinite piezo-laminated cylindrical shell filled with and submerged in compressible fluids was analytically estimated by Rabbani et al. [10].

Effects of poroelastic material on sound transmission, particularly in high frequencies, have been an interesting subject of studies in the recent years. An analytical model was presented by Zhou et al. [11,12] to investigate the effects of external mean flow and exterior turbulent boundary layer on the transmission loss of a double shell lined with poroelastic material. Liu and Hi [13] calculated the transmission loss of random incidence in the diffuse field through double-shell sandwich composite structures with the poroelastic core. Using a mixed

* Corresponding author.
E-mail addresses: orafa@stu.yazd.ac.ir (A.H. Orafa), jalili@yazd.ac.ir (M.M. Jalili), afotuhi@yazd.ac.ir (A.R. Fotuhi).

https://doi.org/10.1016/j.ijnonlinmec.2021.103682
Received 11 July 2020; Received in revised form 18 January 2021; Accepted 18 January 2021
Available online 21 January 2021

Abbreviations

c	Structural damping
c_1	Speed of sound in the external space
c_3	Speed of sound in the internal cavity
f	External pressure
h	Shell thickness
n,m	Mode number
r	Radial coordinates
t	Time
u	Axial displacements
v	Circumferential displacements
w	Radial displacements
x	Axial coordinates
D	Bending stiffness
E	Young's modulus of elasticity
F	Stress Function
H_n^1	Hankel function of first kind
H_n^2	Hankel function of second kind
J_n	Bessel function of first kind
K_{1r}	Radial wave numbers
K_{1x}	Axial wave numbers
L	Shell length
M_x	Bending moment per unit length
N_x	Axial force per unit length
P_r^n	Amplitudes of the reflected waves
P_t^n	Amplitudes of the transmitted waves
P_0	Amplitude of the incident wave
R	Mean shell radius
W^I	Incident sound power
W_n^T	nth term of transmitted sound powers
ν	Poisson's ratio
ρ	Shell density
ρ_1	Density of air in the external space
ρ_3	Density of air in the internal cavity
θ	Circumferential coordinates
Ω	Frequency of the incident wave
ω	Natural frequency
σ	detuning parameter
ψ	Incident wave angle
ζ	Damping ratio

"Biot–Shell" analytical model, Magniez et al. [14] calculated sound transmission through orthotropic sandwich cylinders with a poroelastic core. An extended full method presented based on Biot theory with considering the 3-D wave propagation was developed by Talebitooti et al. [15] to investigate the transmission loss of poroelastic cylindrical shell. They [16] also used this method to study the effect of external subsonic flow on sound transmission through poroelastic cylindrical shell. Using non-dominated sorting genetic algorithm, Talebitooti et al. [17] optimized sound transmission through the laminated composite cylindrical shell with sandwiching a layer of porous material as an intermediate layer.

A large number of studies are available on nonlinear vibrations of circular cylindrical shells. Pellicano et al. [18] investigated non-linear vibration of simply supported circular cylindrical shells considering geometric nonlinearities and the effect of viscous structural damping. Using five classical non-linear shell theories, the response of an empty and simply supported circular cylindrical shell subjected to radial harmonic excitation has been computed by Amabili [19]. The nonlinear vibrations of empty or fluid-filled circular cylindrical shells, clamped at both ends and subjected to a radial harmonic force excitation, have been studied by Karagiozis et al. [20]. Using both Donnell's non-linear theory retaining in-plane displacements and the Sanders–Koiter non-linear theory, Amabili et al. [21] investigated the effect of geometric imperfections on nonlinear stability of circular cylindrical shells conveying incompressible fluid. Sanders–Koiter nonlinear shell theory was used by Kurylov and Amabili [22] to investigate Large-amplitude (geometrically nonlinear) forced vibrations of circular cylindrical shells with different boundary conditions. Alijani and Amabili [23] investigated geometrically nonlinear forced vibrations of water-filled arbitrary laminated circular cylindrical shells using the Amabili–Reddy nonlinear higher-order shear deformation theory. In an experimental–numerical study, Amabili et al. [24] examined nonlinear vibrations of a water-filled circular cylindrical shell subjected to radial harmonic excitation in the spectral neighborhood of the lowest resonances, using a seamless aluminum sample. Semi-analytical solution of nonlinear vibrations of circular cylindrical shell made of carbon nanotube fiber-reinforced composite excited by a radial harmonic force with considering structural damping was studied by Yadav et al. [25].

In most of the literatures reviewed above, although Sound Transmission Loss (STL) across various types of shells has been studied, there has been no investigation on the nonlinear acoustic behavior of the cylindrical shell in contrast to plane sound wave, so far. Therefore, in this paper an analytical approach is developed to study the nonlinear vibro-acoustic behavior of the cylindrical shells based on Donnell's theory. Then, the frequency–response for the radial deflection of the shell and transmission loss through the cylindrical shell due to an oblique plane sound wave are calculated using the method of multiple scales (MMS). MMS has also been used in other nonlinear vibro-acoustic problems to calculate frequency–response of structure vibration and transmission loss [26–28].

The rest of the current paper is organized as follows. In Section 2, the vibro-acoustic model of the sound transmission through a cylindrical shell is presented. Then using the Galerkin method based on the boundary conditions of the system, nonlinear differential equations of the system are achieved. In Section 3, the method of multiple scales is utilized to determine the frequency–response of the shell due to sound wave excitation. In Section 4, results of the current model and their discussion and parametric studies are presented. Finally, conclusions are provided in Section 5.

2. System model

Fig. 1 shows the geometry and coordinate system of a cylindrical shell with thickness h, mean surface radius R and length L considered for the study in this paper. The cylindrical shell is described with the coordinates (x, r, θ), in which x, r and θ denote the axial, radial and circumferential coordinates, respectively. Also, the displacements in the axial, radial and circumferential directions are denoted by $u(x,\theta)$, $w(x,\theta)$ and $v(x,\theta)$, respectively.

Using the Donnell's nonlinear shallow shell theory, partial differential equations of the shell radial motion can be represented as follows [29]:

$$D\nabla^4 w + ch\dot{w} + \rho h\ddot{w} = f + \frac{1}{R}\frac{\partial^2 F}{\partial x^2} + \left(\frac{\partial^2 F}{R^2\partial\theta^2}\frac{\partial^2 w}{\partial x^2} - 2\frac{\partial^2 F}{R\partial x\partial\theta}\frac{\partial^2 w}{R\partial x\partial\theta} + \frac{\partial^2 F}{\partial x^2}\frac{\partial^2 w}{R^2\partial\theta^2}\right) \quad (1)$$

where $D = Eh^3/\left[12\left(1-\nu^2\right)\right]$ is bending stiffness and E and ν are Young's modulus of elasticity and Poisson's ratio, respectively. Also, c and ρ represent the structural damping and density of the shell material and f denotes the external pressure load. The in-plane stress function

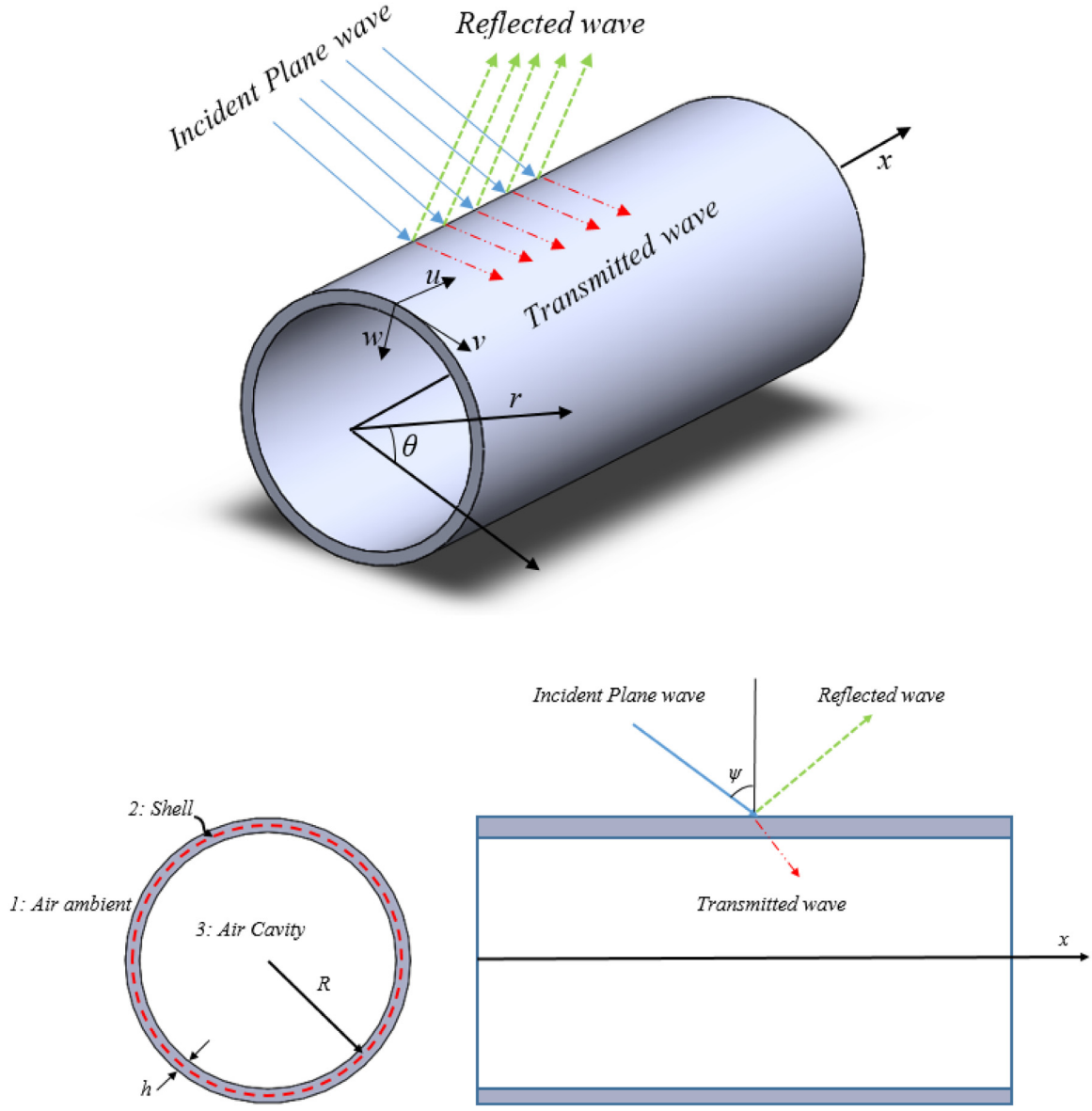

Fig. 1. Schematic representation of the double-walled cylindrical shell system.

F is represented as follows:

$$\frac{1}{Eh}\nabla^4 F = -\frac{1}{R}\frac{\partial^2 w}{\partial x^2} + [\left(\frac{\partial^2 w}{R\partial x\partial\theta}\right)^2 - \frac{\partial^2 w}{\partial x^2}\frac{\partial^2 w}{R^2\partial\theta^2}] \tag{2}$$

The radial displacement w can be expanded by the eigenmodes as follows:

$$w(x.\theta.t) = \left[A_{mn}(t)\cos(n\theta) + B_{mn}(t)\sin(n\theta)\right]\sin\left(\lambda_m x\right) + \sum_{m=1}^{\tilde{N}} A_{m0}(t)\sin\left(\lambda_m x\right) \tag{3}$$

Where n and m are respectively the number of circumferential waves and longitudinal half-waves, $\lambda_m = m\pi/L$ and t is the time. Also, $A_{mn}(t)$, $B_{mn}(t)$ and $A_{m0}(t)$ denote the generalized coordinates that are unknown functions of t. Considering $\tilde{N} = 3$ and $m = 1$, the following mode expansion is obtained [30].

$$w = \left[A_{1n}(t)\cos(n\theta) + B_{1n}(t)\sin(n\theta)\right]\sin\left(\frac{\pi}{L}x\right) + A_{10}(t)\left[3\sin\left(\frac{\pi}{L}x\right) - \sin\left(\frac{3\pi}{L}x\right)\right] \tag{4}$$

where $n \geq 1$. The boundary conditions of the shallow cylinder are defined as follows:

$$\begin{aligned} &w = 0 && \text{at } x = 0; x = L\\ &M_x = -D\left\{\frac{\partial^2 w}{\partial x^2} + \nu\frac{\partial^2 w}{R^2\partial\theta^2}\right\} = 0 && \text{at } x = 0; x = L\\ &N_x = 0 && \text{at } x = 0; x = L\\ &v = 0 && \text{at } x = 0; x = L \end{aligned}$$

where M_x and N_x are the bending moment and the axial force per unit length, respectively.

Substituting Eq. (4) into Eq. (2), the following expression for stress function F can be written.

$$F = F_p + F_h \tag{5}$$

in which F_p and F_h are the particular and homogeneous solutions of Eq. (2) and given by [30]:

$$\begin{aligned} F_p = {} & c_1(t)\cos(n\theta) + c_2(t)\sin(n\theta) + c_3(t)\sin\left(\lambda_1 x\right)\\ & + c_4(t)\cos(n\theta)\sin\left(\lambda_1 x\right) + c_5(t)\sin(n\theta)\sin\left(\lambda_1 x\right)\\ & + c_6(t)\cos\left(2\lambda_1 x\right) + c_7(t)\cos(2n\theta) + c_8(t)\sin(2n\theta)\\ & + c_9(t)\cos(n\theta)\cos\left(2\lambda_1 x\right) + c_{10}(t)\sin(n\theta)\cos\left(2\lambda_1 x\right) \end{aligned}$$

$$+ c_{11}(t)\sin(3\lambda_1 x) + c_{12}(t)\cos(n\theta)\cos(4\lambda_1 x) + c_{13}(t)\sin(n\theta)\cos(4\lambda_1 x) \tag{6a}$$

$$F_h = \frac{1}{2}x^2\left\{-EhA_{10}(t)\frac{16}{3\lambda_1 LR} + [A_{1n}(t)^2 + B_{1n}(t)^2]\frac{n^2}{8R^2} + \frac{2}{L}\lambda_1[c_3(t) + 3c_{11}(t)]\right\} \tag{6b}$$

where functions c_i are defined in Appendix A.

The incident plane wave P_I which satisfies the homogeneous Helmholtz equation in the cylindrical coordinate system can be defined as [31]

$$P_I = P_0\sum_{n=0}^{\infty}\epsilon_n(-j)^n J_n(K_{1r}r)\cos(n\theta)e^{j(\Omega t - K_{1x}x)} \tag{7}$$

where P_0 is the amplitude of the incident sound wave, ϵ_n is the Neumann factor in which $\epsilon_n = 1$ for $n = 0$ and $\epsilon_n = 2$ for $n = 1, 2, 3, \ldots$ and J_n is the Bessel function of the first kind. Also, K_{1r} and K_{1x} are the radial and axial wave numbers, respectively, and can be determined as follows:

$$K_{1r} = \frac{\Omega}{c_1}\cos(\psi)\,;\, K_{1x} = \frac{\Omega}{c_1}\sin(\psi) \tag{8}$$

in which Ω is the frequency of the incident wave, ψ is the incident angle and c_1 is the speed of sound in the external space of the shell. Also, the waves reflected and transmitted from and through the cylindrical shell can be represented as:

$$P_R = \sum_{n=0}^{\infty}P_r^n H_n^2(K_{1r}r)\cos(n\theta)e^{j(\Omega t - K_{1x}x)} \tag{9}$$

$$P_T = \sum_{n=0}^{\infty}P_t^n H_n^1(K_{3r}r)\cos(n\theta)e^{j(\Omega t - K_{3x}x)} \tag{10}$$

where P_r^n and P_t^n are the unknown complex amplitudes of the reflected and transmitted waves, respectively. The longitudinal and radial sound wavenumbers in the transmission field can be expressed as:

$$K_{3x} = K_{1x};\, K_{3r} = \sqrt{\left(\frac{\Omega}{c_3}\right)^2 - K_{3x}^2} \tag{11}$$

where c_3 is the speed of sound in the internal cavity of the shell.

Moreover, the relationships between pressure and radial displacement can be expressed as:

$$\frac{\partial(P_I + P_R)}{\partial r} = -\rho_1\frac{\partial^2 w}{\partial t^2}\text{at}r = R \tag{12}$$

$$\frac{\partial(P_T)}{\partial r} = -\rho_3\frac{\partial^2 w}{\partial t^2}\text{at}r = R \tag{13}$$

Substituting Eqs. (4), (7) and (9) into Eq. (12) and applying the Galerkin method with suitable weighting functions Z_s, two algebraic equations can be obtained for the variables P_r^n and P_r^0. The weighting functions Z_s are defined as:

$$\begin{aligned} Z_s &= cos(n\theta)\,sin\left(\frac{\pi}{L}x\right);\, s = 1\\ Z_s &= sin(n\theta)\,sin\left(\frac{\pi}{L}x\right);\, s = 2\\ Z_s &= 3sin\left(\frac{\pi}{L}x\right) - sin\left(\frac{3\pi}{L}x\right);\, s = 3 \end{aligned} \tag{14}$$

The results of the Galerkin projection can be represented as:

$$\begin{aligned} &\{2P_0(-j)^n J_n'(K_{1r}r) + P_r^n H_n^{2\prime}(K_{1r}r)\}\frac{L\pi^2 e^{j\Omega t}\left(1 + e^{-jK_{1x}L}\right)}{\pi^2 - L^2K_{1x}^2} = -\frac{\rho_1\pi L}{2}\ddot{A}_{1n}(t) && s = 1\\ &0 && s = 2\\ &\{P_0J_0'(K_{1r}r) + \Pr 0\,H_0^{2\prime}(K_{1r}r)\}\left(\frac{-1}{9\pi^2 - L^2K_{1x}^2} + \frac{1}{\pi^2 - L^2K_{1x}^2}\right)\\ &\quad\times 6L\pi^2 e^{j\Omega t}(1 + e^{-jK_{1x}L}) = -10\rho_1\pi L\ddot{A}_{10}(t) && s = 3 \end{aligned} \tag{15}$$

Solving Eq. (15), variables P_r^n and P_r^0 can be obtained as follows:

$$\begin{aligned} P_r^n &= -\frac{\rho_1\pi L}{2}\frac{(\pi^2 - L^2K_{1x}^2)e^{-j\Omega t}}{L\pi^2\left(1 + e^{-jK_{1x}L}\right)H_n^{2\prime}(K_{1r}r)}\ddot{A}_{1n}(t) - \frac{2P_0(-j)^n J_n'(K_{1r}r)}{H_n^{2\prime}(K_{1r}r)} && s = 1\\ \Pr 0 &= \frac{-10\rho_1\pi L\ddot{A}_{10}(t)e^{-j\Omega t}}{6(\frac{-1}{9\pi^2 - L^2K_{1x}^2} + \frac{1}{\pi^2 - L^2K_{1x}^2})L\pi^2(1 + e^{-jK_{1x}L})H_0^{2\prime}(K_{1r}r)} - \frac{P_0J_0'(K_{1r}r)}{H_0^{2\prime}(K_{1r}r)} && s = 3 \end{aligned} \tag{16}$$

Similarly, with substituting Eqs. (4) and (10) into Eq. (13) and using the Galerkin projection with weighting functions Z_s, the following relations are obtained:

$$\begin{aligned} &P_t^n H_n^{1\prime}(K_{3r}r)\frac{L\pi^2 e^{j\Omega t}\left(1 + e^{-jK_{3x}L}\right)}{\pi^2 - L^2K_{3x}^2} = -\frac{\rho_3\pi L}{2}\ddot{A}_{1n}(t) && s = 1\\ &0 && s = 2\\ &P_t^0 H_0^{1\prime}(K_{3r}r)\left(\frac{-1}{9\pi^2 - L^2K_{3x}^2} + \frac{1}{\pi^2 - L^2K_{3x}^2}\right)\\ &\quad\times 6L\pi^2 e^{j\Omega t}\left(1 + e^{-jK_{3x}L}\right) = -10\rho_3\pi L\ddot{A}_{10}(t) && s = 3 \end{aligned} \tag{17}$$

Eq. (17) can be solved for the variables P_t^n and P_t^0 as function of generalized coordinates.

$$\begin{aligned} P_t^n &= -\frac{\rho_3\pi L}{2}\frac{(\pi^2 - L^2K_{3x}^2)e^{-j\Omega t}}{L\pi^2\left(1 + e^{-jK_{3x}L}\right)H_n^{1\prime}(K_{3r}r)}\ddot{A}_{1n}(t) && s = 1\\ P_t^0 &= \frac{-10\rho_3\pi Le^{-j\Omega t}}{6(\frac{-1}{9\pi^2 - L^2K_{3x}^2} + \frac{1}{\pi^2 - L^2K_{3x}^2})L\pi^2(1 + e^{-jK_{3x}L})H_0^{1\prime}(K_{3r}r)}\ddot{A}_{10}(t) && s = 3 \end{aligned} \tag{18}$$

External pressure load f can be expressed as follows:

$$f = P_I^1 + P_R^1 - P_T^3 \tag{19}$$

Substituting Eqs. (7), (9) and (10) into Eq. (19), the following relation can be obtained for pressure load f.

$$f = \sum_{n=0}^{\infty}[P_0\epsilon_n(-j)^n J_n(K_{1r}r) + P_r^n H_n^2(K_{1r}r) - P_t^n H_n^1(K_{3r}r)]\cos(n\theta)e^{j(\omega t - K_{1x}x)} \tag{20}$$

Applying Galerkin projection with weighting functions Z_s to Eq. (1), the following system of second-order ordinary differential equations are obtained:

$$\ddot{A}_{1n}(t) + P_1A_{1n}(t) = P_2c\dot{A}_{1n}(t) + P_3A_{1n}A_{10} + P_4A_{1n}^3 + P_4A_{1n}B_{1n}^2 + P_5A_{1n}A_{10}^2 + P_6\cos(\Omega t + \varnothing_1) \tag{21}$$

$$\ddot{B}_{1n}(t) + Q_1B_{1n}(t) = Q_2c\dot{B}_{1n}(t) + Q_3B_{1n}A_{10} + Q_4B_{1n}^3 + Q_4B_{1n}A_{1n}^2 + Q_5B_{1n}A_{10}^2 \tag{22}$$

$$\ddot{A}_{10}(t) + \Pi_1A_{10}(t) = \Pi_2c\dot{A}_{10}(t) + \Pi_3A_{1n}^2 + \Pi_3B_{1n}^2 + \Pi_4A_{1n}^2A_{10} + \Pi_4B_{1n}^2A_{10} + \Pi_6cos(\Omega t + \varnothing_2) \tag{23}$$

The coefficients of Eqs. (21) to (23) are defined in Appendix B.

3. Solution method

In this section, the method of multiple scales (MMS) is employed to find an analytical solution for the frequency–response of the proposed nonlinear vibro-acoustic model. In this approach, the response can be presented by an expansion which is a function of multiple-independent

scales T_i. According to this method, the solution of Eqs. (21) to (23) can be represented by an expansion having the form [32]

$$\begin{aligned} A_{1n}(T_0) &= \varepsilon u_{11}(T_0;T_1;T_2) + \varepsilon^2 u_{12}(T_0;T_1;T_2) + \varepsilon^3 u_{13}(T_0;T_1;T_2) \\ B_{1n}(T_0) &= \varepsilon u_{21}(T_0;T_1;T_2) + \varepsilon^2 u_{22}(T_0;T_1;T_2) + \varepsilon^3 u_{23}(T_0;T_1;T_2) \\ A_{10}(T_0) &= \varepsilon u_{31}(T_0;T_1;T_2) + \varepsilon^2 u_{32}(T_0;T_1;T_2) + \varepsilon^3 u_{33}(T_0;T_1;T_2) \end{aligned} \tag{24}$$

where ε is a small dimensionless parameter and $T_n = \varepsilon^n t$ are time scales. Hence the time derivative is transformed into

$$\begin{aligned} \frac{d}{dt} &= D_0 + \varepsilon D_1 + \dots \\ \frac{d^2}{dt^2} &= {D_0}^2 + 2D_0D_1\varepsilon + (D_1^2 + 2D_0D_2)\varepsilon^2 + \dots \end{aligned} \tag{25}$$

in which $D_n = \frac{\partial}{\partial T_n}$.

Considering $c = \varepsilon^2\hat{c}$, $P_6 = \varepsilon^3\hat{P}_6$ and $\Pi_6 = \varepsilon^3\hat{\Pi}_6$, substituting Eqs. (24) and (25) into Eqs. (21)–(23) and equating the coefficients of identical powers of ε to zero, one acquires:

ε^1:

$${D_0}^2u_{11} + P_1u_{11} = 0 \tag{26a}$$

$${D_0}^2u_{21} + Q_1u_{21} = 0 \tag{26b}$$

$${D_0}^2u_{31} + \Pi_1u_{31} = 0 \tag{26c}$$

ε^2:

$${D_0}^2u_{12} + P_1u_{12} = P_3u_{31}u_{11} - 2D_0D_1u_{11} \tag{27a}$$

$${D_0}^2u_{22} + Q_1u_{22} = Q_3u_{31}u_{21} - 2D_0D_1u_{21} \tag{27b}$$

$${D_0}^2u_{32} + \Pi_1u_{32} = -2D_0D_1u_{31} + \Pi_3{u_{11}}^2 + \Pi_3{u_{21}}^2 \tag{27c}$$

ε^3:

$$\begin{aligned} {D_0}^2u_{13} + P_1u_{13} = &-2D_0D_1u_{12} - (D_1^2 + 2D_0D_2)u_{11} + P_2\hat{c}D_0u_{11} + P_3u_{32}u_{11} \\ &+ P_3u_{12}u_{31} + P_4u_{11}^3 + P_4u_{11}{u_{21}}^2 + P_5u_{11}{u_{31}}^2 \\ &+ \hat{P}_6cos(\Omega t + \varnothing_1) \end{aligned} \tag{28a}$$

$$\begin{aligned} {D_0}^2u_{23} + Q_1u_{23} = &-2D_0D_1u_{22} - (D_1^2 + 2D_0D_2)u_{21} + Q_2\hat{c}D_0u_{21} \\ &+ Q_3u_{21}u_{32} + Q_3u_{22}u_{31} + Q_4{u_{21}}^3 + Q_4u_{21}{u_{11}}^2 \\ &+ Q_5u_{21}{u_{31}}^2 \end{aligned} \tag{28b}$$

$$\begin{aligned} {D_0}^2u_{33} + \Pi_1u_{33} = &-2D_0D_1u_{32} - (D_1^2 + 2D_0D_2)u_{31} + \Pi_2\hat{c}D_0u_{31} \\ &+ 2\Pi_3u_{11}u_{12} + 2\Pi_3u_{21}u_{22} + \Pi_4{u_{11}}^2u_{31} + \Pi_4{u_{21}}^2u_{31} \\ &+ \hat{\Pi}_6cos(\Omega t + \varnothing_2) \end{aligned} \tag{28c}$$

The solution of Eq. (26) can be presented as follows:

$$u_{11} = X_1(T_1.T_2)\,e^{j\omega_1T_0} + \overline{X}_1(T_1.T_2)\,e^{-j\omega_1T_0} \tag{29a}$$

$$u_{21} = X_2(T_1.T_2)\,e^{j\omega_2T_0} + \overline{X}_2(T_1.T_2)\,e^{-j\omega_2T_0} \tag{29b}$$

$$u_{31} = X_3(T_1.T_2)\,e^{j\omega_3T_0} + \overline{X}_3(T_1.T_2)\,e^{-j\omega_3T_0} \tag{29c}$$

in which

$$\omega_1 = \sqrt{P_1}, \omega_2 = \sqrt{Q_1}, \omega_3 = \sqrt{\Pi_1} \tag{30}$$

Substituting the solutions into Eq. (27) yields:

$$\begin{aligned} {D_0}^2u_{12} + {\omega_1}^2u_{12} = &P_3\left(X_3(T_1.T_2)\,X_1(T_1.T_2)\,e^{j(\omega_1+\omega_3)T_0}\right. \\ &\left. + \overline{X}_3(T_1.T_2)\,X_1(T_1.T_2)\,e^{j(\omega_1-\omega_3)T_0}\right) \\ &- 2j\omega_1D_1X_1(T_1.T_2)\,e^{j\omega_1T_0} + cc \end{aligned} \tag{31a}$$

$$\begin{aligned} {D_0}^2u_{22} + {\omega_2}^2u_{22} = &Q_3\left(X_3(T_1.T_2)\,X_2(T_1.T_2)\,e^{j(\omega_2+\omega_3)T_0}\right. \\ &\left. + \overline{X}_3(T_1.T_2)\,X_2(T_1.T_2)\,e^{j(\omega_2-\omega_3)T_0}\right) \\ &- 2j\omega_2D_1X_2(T_1.T_2)\,e^{j\omega_2T_0} + cc \end{aligned} \tag{31b}$$

$$\begin{aligned} {D_0}^2u_{32} + {\omega_3}^2u_{32} = &+\Pi_3({X_1}^2(T_1.T_2)\,e^{2j\omega_1T_0} + X_1\overline{X}_1) \\ &+ \Pi_3({X_2}^2(T_1.T_2)\,e^{2j\omega_2T_0} + X_2\overline{X}_2) \\ &- 2j\omega_3D_1X_3(T_1.T_2)\,e^{j\omega_3T_0} + cc \end{aligned} \tag{31c}$$

To eliminate secular terms from Eq. (31), we must put $D_1X_1 = 0$, $D_1X_2 = 0$ and $D_1X_3 = 0$. It follows that:

$$u_{12} = \frac{P_3X_1X_3}{{\omega_1}^2 - (\omega_1+\omega_3)^2}e^{j(\omega_1+\omega_3)T_0} + \frac{P_3X_1\overline{X}_3}{{\omega_1}^2 - (\omega_1-\omega_3)^2}e^{j(\omega_1-\omega_3)T_0} + cc \tag{32a}$$

$$u_{22} = \frac{Q_3X_2X_3}{{\omega_2}^2 - (\omega_2+\omega_3)^2}e^{j(\omega_2+\omega_3)T_0} + \frac{Q_3X_2\overline{X}_3}{{\omega_2}^2 - (\omega_2-\omega_3)^2}e^{j(\omega_2-\omega_3)T_0} + cc \tag{32b}$$

$$u_{32} = \frac{\Pi_3{X_1}^2}{{\omega_3}^2 - 4{\omega_1}^2}e^{j(2\omega_1T_0)} + \frac{\Pi_3X_1\overline{X}_1}{{\omega_3}^2} + \frac{\Pi_3{X_2}^2}{{\omega_3}^2 - 4{\omega_2}^2}e^{j(2\omega_2T_0)} + \frac{\Pi_3X_2\overline{X}_2}{{\omega_3}^2} + cc \tag{32c}$$

To study the case of primary resonance and state closeness of Ω to ω_1, the detuning parameter σ_1 is introduced as follows:

$$\Omega = \omega_1 + \varepsilon^2\sigma_1 \tag{33}$$

Substituting Eqs. (29), (32) and (33) into Eq. (28), and eliminating secular terms from the resulting equations yields

$$\begin{aligned} &-2j\omega_1D_2X_1 + P_2\hat{c}j\omega_1X_1 + P_3\left(\frac{2\Pi_3{X_1}^2\overline{X}_1}{{\omega_3}^2} + \frac{2\Pi_3X_1X_2\overline{X}_2}{{\omega_3}^2}\right. \\ &\left. + \frac{\Pi_3{X_1}^2\overline{X}_1}{{\omega_3}^2 - 4{\omega_1}^2} + \frac{P_3X_1\overline{X}_3X_3}{{\omega_1}^2 - (\omega_1+\omega_3)^2} + \frac{P_3X_1X_3\overline{X}_3}{{\omega_1}^2 - (\omega_1-\omega_3)^2}\right) \\ &+ P_4(3{X_1}^2\overline{X}_1 + 2X_1X_2\overline{X}_2) + P_5(2X_1X_3\overline{X}_3) \\ &+ \frac{1}{2}\hat{P}_6e^{j(\sigma_1T_2+\varnothing_1)} = 0 \end{aligned} \tag{34}$$

$$\begin{aligned} &-2j\omega_2D_2X_2 + Q_2\hat{c}j\omega_2X_2 + Q_3\left(\frac{2\Pi_3X_2X_1\overline{X}_1}{{\omega_3}^2} + \frac{2\Pi_3{X_2}^2\overline{X}_2}{{\omega_3}^2}\right. \\ &\left. + \frac{\Pi_3{X_2}^2\overline{X}_2}{{\omega_3}^2 - 4{\omega_2}^2} + \frac{Q_3X_2X_3\overline{X}_3}{{\omega_2}^2 - (\omega_2+\omega_3)^2} + \frac{Q_3X_2X_3\overline{X}_3}{{\omega_2}^2 - (\omega_2-\omega_3)^2}\right) \\ &+ Q_4(3{X_2}^2\overline{X}_2 + 2X_2X_1\overline{X}_1) + Q_5(2X_2X_3\overline{X}_3) = 0 \end{aligned} \tag{35}$$

$$\begin{aligned} &-2j\omega_3D_2X_3 + \Pi_2\hat{c}j\omega_3X_3 + 2\Pi_3\left(\frac{P_3X_1\overline{X}_1\overline{X}_3}{{\omega_1}^2 - (\omega_1+\omega_3)^2} + \frac{P_3X_1\overline{X}_1\overline{X}_3}{{\omega_1}^2 - (\omega_1-\omega_3)^2}\right. \\ &\left. + \frac{Q_3X_3X_2\overline{X}_2}{{\omega_2}^2 - (\omega_2+\omega_3)^2} + \frac{Q_3X_3X_2\overline{X}_2}{{\omega_2}^2 - (\omega_2-\omega_3)^2}\right) \\ &+ \Pi_4\left(2X_3X_1\overline{X}_1 + 2X_3X_2\overline{X}_2\right) = 0 \end{aligned} \tag{36}$$

Inserting the polar form $X_i = \frac{1}{2}x_ie^{j\beta_i}$ into Eqs. (34) to (36) and separating the real and imaginary parts, we have:

$$\begin{aligned} &8\omega_1x_1(\sigma_1 - {\gamma_1}') + P_3\left(\frac{2\Pi_3{x_1}^3}{{\omega_3}^2} + \frac{2\Pi_3x_1{x_2}^2}{{\omega_3}^2} + \frac{\Pi_3{x_1}^3}{{\omega_3}^2 - 4{\omega_1}^2}\right. \\ &\left. + \frac{P_3x_1{x_3}^2}{{\omega_1}^2 - (\omega_1+\omega_3)^2} + \frac{P_3x_1{x_3}^2}{{\omega_1}^2 - (\omega_1-\omega_3)^2}\right) + P_4(3{x_1}^3 + 2x_1{x_2}^2) \\ &+ P_5(2x_1{x_3}^2) + 4\hat{P}_6cos(\gamma_1) = 0 \end{aligned} \tag{37a}$$

$$-2\omega_1{x_1}' + P_2\hat{c}\omega_1x_1 + \hat{P}_6sin(\gamma_1) = 0 \tag{37b}$$

$$\begin{aligned} &8\omega_2x_2{\beta_2}' + Q_3\left(\frac{2\Pi_3x_2{x_1}^2}{{\omega_3}^2} + \frac{2\Pi_3{x_2}^3}{{\omega_3}^2} + \frac{\Pi_3{x_2}^3}{{\omega_3}^2 - 4{\omega_2}^2} + \frac{Q_3x_2{x_3}^2}{{\omega_2}^2 - (\omega_2+\omega_3)^2}\right. \\ &\left. + \frac{Q_3x_2{x_3}^2}{{\omega_2}^2 - (\omega_2-\omega_3)^2}\right) + Q_4(3{x_2}^3 + 2x_2{x_1}^2) + Q_5(2x_2{x_3}^2) = 0 \end{aligned} \tag{38a}$$

$$-2\omega_2{x_2}' + Q_2\hat{c}\omega_2x_2 = 0 \tag{38b}$$

$$\begin{aligned} &8\omega_3x_3{\beta_3}' + 2\Pi_3\left(\frac{P_3x_3{x_1}^2}{{\omega_1}^2 - (\omega_1+\omega_3)^2} + \frac{P_3x_3{x_1}^2}{{\omega_1}^2 - (\omega_1-\omega_3)^2}\right. \\ &\left. + \frac{Q_3x_3{x_2}^2}{{\omega_2}^2 - (\omega_2+\omega_3)^2} + \frac{Q_3x_3{x_2}^2}{{\omega_2}^2 - (\omega_2-\omega_3)^2}\right) \\ &+ \Pi_4\left(2x_3{x_1}^2 + 2x_3{x_2}^2\right) = 0 \end{aligned} \tag{39a}$$

$$-2\omega_3 x_3{}' + \Pi_2 \hat{c}\omega_3 x_3 = 0 \tag{39b}$$

where $\gamma_1 = \sigma_1 T_2 - \beta_1 + \varnothing_1$. The steady-state motions correspond to $x_1{}' = x_2{}' = x_3{}' = \gamma_1{}' = \beta_2' = \beta_3' = 0$. It follows that $x_2 = x_3 = 0$ and

$$8\omega_1 x_1 \sigma_1 + P_3\left(\frac{2\Pi_3 {x_1}^3}{{\omega_3}^2} + \frac{\Pi_3 {x_1}^3}{{\omega_3}^2 - 4{\omega_1}^2}\right) + P_4\left(3{x_1}^3\right) + 4\hat{P}_6 \cos\left(\gamma_1\right) = 0 \tag{40a}$$

$$4P_2\hat{c}\omega_1 x_1 + 4\hat{P}_6 \sin\left(\gamma_1\right) = 0 \tag{40b}$$

Eliminating γ_1 from Eq. (40) leads to the frequency–response equation as follows:

$${g_1}^2 {x_1}^6 + 16\omega_1 g_1 \sigma_1 {x_1}^4 + \left(64{\omega_1}^2{\sigma_1}^2 + 16P_2^2\hat{c}^2{\omega_1}^2\right){x_1}^2 = 16\hat{P}_6^2 \tag{41}$$

where

$$g_1 = P_3\left(\frac{2\Pi_3}{{\omega_3}^2} + \frac{\Pi_3}{{\omega_3}^2 - 4{\omega_1}^2}\right) + 3P_4 \tag{42}$$

Similar to case $\Omega \approx \omega_1$, the frequency–response equation for the case $\Omega = \omega_3 + \varepsilon^2\sigma_3$ can be obtained as follows:

$$\left(64{\omega_3}^2\sigma_3^2 + 16{\Pi_2}^2\hat{c}^2{\omega_3}^2\right){x_3}^2 = 16\hat{\Pi}_6^2 \tag{43}$$

Where $\Pi_6 = \varepsilon^3\hat{\Pi}_6$.

Here, the stability of different portions of the response curve about $\Omega \approx \omega_1$ are determined by investigating the nature of the singular points of Eq. (37). To accomplish this, consider the following relations:

$$x_1 = x_{10} + x_{11}, \gamma_1 = \gamma_{10} + \gamma_{11} \tag{44}$$

Substituting Eq. (44) into Eq. (37), expanding for small x_{11} and γ_{11}, noting that x_{10} and γ_{10} satisfy Eq. (37), and keeping linear terms in x_{11} and γ_{11}, one obtains:

$$\begin{aligned}
\gamma_{11}{}' &= \left(\frac{g_1 x_{10}}{4\omega_1} - \frac{\hat{P}_6 cos(\gamma_{10})}{2\omega_1 {x_{10}}^2}\right)x - \frac{\hat{P}_6 sin(\gamma_{10})}{2\omega_1 x_{10}}\gamma_{11} \\
x_{11}{}' &= \frac{P_2\hat{c}}{2}x + \frac{\hat{P}_6 cos(\gamma_{10})}{2\omega_1}\gamma_{11}
\end{aligned} \tag{45}$$

Therefore, the stability of the steady-state motion can be investigated based on the eigenvalues of the coefficients matrix on the right-hand side of Eq. (45). Using Eq. (40b), one can obtain the following eigenvalue equation:

$$\left|\lambda - \frac{P_2\hat{c}}{2} - \left(\frac{g_1 x_0}{4\omega_1} - \frac{\hat{P}_6 cos(\gamma_0)}{2\omega_1 {x_0}^2}\right) - \frac{\hat{P}_6 cos(\gamma_0)}{2\omega_1}\lambda - \frac{P_2\hat{c}}{2}\right| = 0 \tag{46}$$

Expanding the determinant yields:

$$\lambda^2 - 2\left(\frac{P_2\hat{c}}{2}\right)\lambda + \left(\frac{P_2\hat{c}}{2}\right)^2 - \left(\frac{g_1 x_0}{4\omega_1} - \frac{\hat{P}_6 cos\left(\gamma_0\right)}{2\omega_1 {x_0}^2}\right)\left(\frac{\hat{P}_6 cos\left(\gamma_0\right)}{2\omega_1}\right) = 0 \tag{47}$$

The stability of the singular points and hence the steady-state solutions are determined by the real parts of the roots of Eq. (47). The steady-state solution is stable if the real part of each root is negative or zero. If the real part of at least one of the roots is positive definite, the corresponding steady-state solution is unstable. The roots of Eq. (47) are as follows:

$$\lambda = \left(\frac{P_2\hat{c}}{2}\right) \pm \sqrt{\left(\frac{P_2\hat{c}}{2}\right)^2 + \left(\frac{g_1 x_0}{4\omega_1} - \frac{\hat{P}_6 cos\left(\gamma_0\right)}{2\omega_1 {x_0}^2}\right)\left(\frac{\hat{P}_6 cos\left(\gamma_0\right)}{2\omega_1}\right)} \tag{48}$$

Note that $\left(\frac{P_2\hat{c}}{2}\right) < 0$; hence, the steady-state motions are unstable when

$$\left(\frac{g_1 x_0}{4\omega_1} - \frac{\hat{P}_6 cos\left(\gamma_0\right)}{2\omega_1 {x_0}^2}\right)\left(\frac{\hat{P}_6 cos\left(\gamma_0\right)}{2\omega_1}\right) > 0 \tag{49}$$

4. Sound transmission loss

The sound transmission loss is defined as the ratio of the incident sound powers and the transmitted sound powers through unit length of the shell along the axial direction.

$$TL = 10\log_{10}\left(\frac{W^I}{\sum_{n=0}^{\infty} W_n^T}\right) \tag{50}$$

in which W^I is incident sound power and W_n^T is the nth term of transmitted sound powers corresponding to the nth mode and can be defined as follows [33]:

$$W^I = R\frac{{P_0}^2 cos(\psi)}{\rho_1 c_1} \tag{51}$$

$$W_n^T = \frac{1}{2}Real\{\int_0^{2\pi}\int_0^L P_T^3 \frac{\partial w}{\partial t} dx d\theta\} \tag{52}$$

For case $\Omega \approx \omega_1$, substituting Eqs. (4) and (10) into Eq. (52) yields:

$$\begin{aligned}
W_n^T = \frac{1}{2}Real\{&\int_0^1\int_0^{2\pi} P_t^n H_n^1\left(K_{3r}r\right)\cos\left(n\theta\right) e^{j(\Omega t - K_{3x}x)}\frac{\partial}{\partial t} \\
&\times \left(\left[A_{1n}(t)cos\left(n\theta\right) + B_{1n}(t)sin\left(n\theta\right)\right]\sin\left(\frac{\pi}{L}x\right)\right. \\
&\left. + A_{10}\left(t\right)\left[3\sin\left(\frac{\pi}{L}x\right) - \sin\left(\frac{3\pi}{L}x\right)\right]\right) d\theta dx\}
\end{aligned} \tag{53}$$

Performing some mathematical calculations, Eq. (53) can be rewritten as follows:

$$W_n^T = \frac{\pi}{2}Real\{\int_0^1 P_t^n H_n^1\left(K_{3r}r\right) e^{j(\Omega t - K_{3x}x)}\dot{A}_{1n}(t)\sin\left(\frac{\pi}{L}x\right) dx\} \tag{54}$$

Substituting Eq. (18) into Eq. (48) yields:

$$W_n^T = -\frac{\pi\rho_3}{4}Real\{\dot{A}_{1n}(t)\ddot{A}_{1n}\left(t\right)\frac{H_n^1\left(K_{3r}r\right)}{H_n^{1\prime}(K_{3r}r)}\} \tag{55}$$

Similar to case $\Omega \approx \omega_1$, from Eq. (24), $A_{1n}\left(t\right)$ can be calculated as follows:

$$\begin{aligned}
&A_{1n}\left(t\right) = \varepsilon u_{11} = \varepsilon X_1\left(T_2\right)e^{j\omega_1 t} + \varepsilon\overline{X}_1\left(T_2\right)e^{-j\omega_1 T_0} = \\
&\varepsilon\left(\frac{1}{2}x_1 e^{j(\omega_1 t + \beta_1)} + \frac{1}{2}x_1 e^{-j(\omega_1 t + \beta_1)}\right) = \varepsilon x_1\cos\left(\omega_1 t + \beta_1\right)
\end{aligned} \tag{56}$$

Substituting Eq. (56) into Eq. (55), the following relation can be obtained for W_n^T:

$$W_n^T = \left|\frac{\pi\rho_3}{8}\Omega^3 u^2 Real\{\frac{H_n^1\left(K_{3r}r\right)}{H_n^{1\prime}(K_{3r}r)}\}\right| \tag{57}$$

Therefore, according to Eqs. (51) and (57) the transmission loss of the shell is calculated as follows:

$$TL = 10\log_{10}\left(\frac{8{P_0}^2 cos(\psi)}{\left|\pi\rho_1 c_1\rho_3\Omega^3 u^2 Real\{\frac{H_n^1(K_{3r}r)}{H_n^{1\prime}(K_{3r}r)}\}\right|}\right) \tag{58}$$

Similar to case $\Omega \approx \omega_1$, the transmission loss for the case $\Omega \approx \omega_3$ can be obtained as follows:

$$TL = 10\log_{10}\left(\frac{2{P_0}^2 cos(\psi)}{\left|5\pi\rho_1 c_1\rho_3\Omega^3 u^2 Real\{\frac{H_0^1(K_{3r}r)}{H_0^{1\prime}(K_{3r}r)}\}\right|}\right) \tag{59}$$

5. Simulations, results and discussion

To validate the model presented in this paper, its predictions of the responses are compared with the numerical results reported by Amabili et al. [30]. In this reference, nonlinear vibration of a simply supported circular cylindrical shell was analyzed. The shell characteristics in this reference are: $L = 0.2$ m, $R = 0.1$ m, $h = 0.247 \times 10^{-3}$ m, $E = 71.02 \times 10^9$ Pa, $\rho = 2796\ \frac{\text{kg}}{\text{m}^3}$, $\upsilon = 0.31$. Also, the damping ratio and the amplitude of the external excitation are considered $2\zeta = 0.001$ and $f_{mn} = 0.0012h^2\rho\omega_{mn}^2$, respectively, and the driven mode is associated with $n = 6$ and $m = 1$. In Fig. 2, the frequency–response of the driven mode is shown and compared to that obtained by Amabili et al. [30]. This figure shows good agreement between the present results and those presented in Ref. [30].

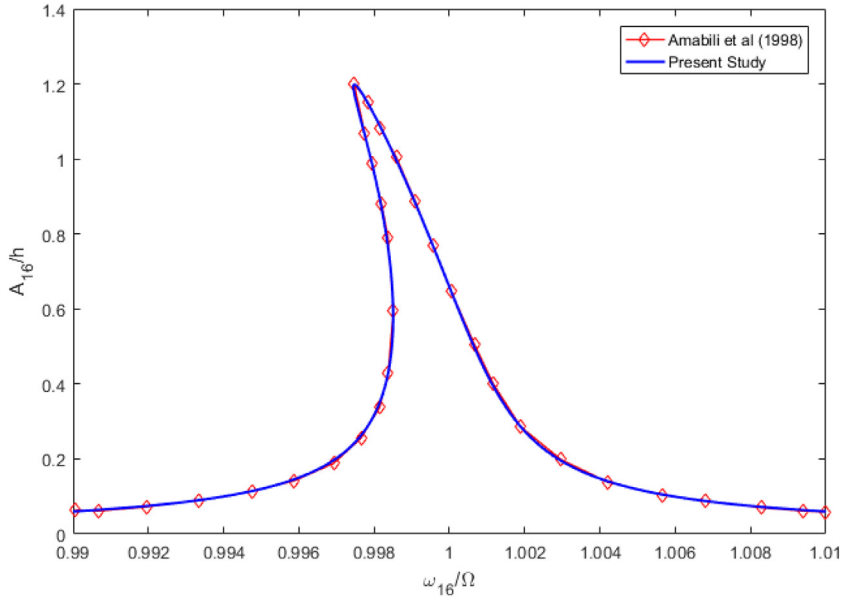

Fig. 2. Comparison of the frequency–response of the shell for the driven mode ($n = 6$ and $m = 1$) with Amabili et al. [30].

Table 1
The basic simulation conditions used in the present study.

Parameter	Value	Parameter	Value
P_0	210 dB (8.6 MPa)	L	1 (m)
ρ_1	0.9389 (Kg/m^3)	h	1 (mm)
ρ_3	1.21 (Kg/m^3)	ν	0.3
c_1	388 (m/s)	ρ	7750 (Kg/m^3)
c_3	343 (m/s)	ψ	45°
E	190 (GPa)	ζ	0.001
R	0.1 (m)		

5.1. Primary resonance and stability analysis

In this section, effects of different parameters on frequency–response function of the system are investigated. The specifications of the cylindrical shell investigated in this paper are listed in Table 1.

To verify the MMS approximate solution of the nonlinear equations presented in this paper, the approximate analytical solution for shell response induced by the acoustic excitations is compared with the numerical one, which was calculated using the Runge–Kutta method. Fig. 3 shows the steady state time response of A_{11} when the frequency of the incident sound wave is close to ω_1. Also, the comparison between the MMS and numerical solutions for the steady state time response of A_{10} about excitation frequency ω_3 is presented in Fig. 4. As displayed in these figures, good agreement is observed between the MMS approximation and numerical solutions.

For the case of primary resonance ($\Omega \approx \omega_1$), the frequency–response of the shell vibration and its transmission loss are presented in Figs. 5 and 6, respectively. Also, using the steady state time response for different frequencies of the incident sound wave calculated by the Runge–Kutta numerical method, the frequency–response and TL are obtained and depicted in these figures. The comparison between the numerical and the MMS approximation results shows good correlation.

As it is observed in Fig. 7, increasing the detuning parameter from point A to point C leads to a gradual increase in steady state vibration amplitude. At point C, upward jump occurs to point D. After that, by increasing the detuning parameter, vibration amplitude decreases. On the other hand, as σ is decreased from point E to F, steady state vibration amplitude increases; and at point F, there is a downward jump to the point B. According to Fig. 8, the bending of the TL curve about the natural frequency of the linear system (ω_1) is responsible for a jump phenomenon in this curve. If the detuning parameter is slowly decreased from point E, a jump from point F to point B takes place. Also, if this parameter is increased from point A, a jump from point C to point D takes place and point D is the resonant frequency.

Frequency responses of vibration and transmission loss curves of the cylindrical shell in the primary resonance case $\Omega \approx \omega_1$ for different incident sound amplitudes are illustrated in Fig. 9(a) and (b), respectively. According to these figures, for the primary resonance cases, with an increase in the incident sound amplitude, the amplitude of steady state vibration increases. It can be observed from Fig. 9(b) that in the case of increasing the detuning parameter, increasing the amplitude of the incident wave increases the transmission loss through the shell about the natural frequency of the linear system. By getting away from this frequency, excitation level would incorporate no effect on the TL. In the case of decreasing the detuning parameter, the amplitude of the incident wave has no effect on the minimum transmission loss through the cylindrical shell. However, with an increase in the incident sound amplitude, the frequency of the minimum transmission loss decreases.

Based on stability analysis Eq. (49) for nonlinear model, the real part of the eigenvalues of fixed points are plotted in Fig. 9(c). As it is shown, some fixed points of the system with incident sound amplitudes 190, 200 and 210 dB produce purely real eigenvalues with opposite signs. Hence, the responses corresponding to those saddle points are unstable and unrealizable in any experiment. Consequently, the shell vibration under incident sound amplitude 190–210 dB experiences jump phenomena by considering nonlinear model.

The effect of damping ratio on frequency–response function and transmission loss for primary resonance case $\Omega \approx \omega_1$ is presented in Fig. 10(a) and (b), respectively, in which the damping ratio is defined as $\zeta = \frac{c}{(2\rho\omega_1)}$. According to these figures in both cases, with the increase in damping ratio, the bending of the curves decreases and resonance frequency approaches the natural frequency of the linear system. It is observed that utilizing material with more damping ratio has positive effects on the noise reduction of the cylindrical shell around the natural frequency $\Omega \approx \omega_1$. As depicted in Fig. 10(b), increasing the damping ratio from 0.001 to 0.01 increases the maximum value of the transmission loss about 27% and 111% for the case of increasing and decreasing the detuning parameter, respectively, which is a great achievement because sound transmits easily through a structure at its critical frequency. Therefore, obtaining high transmission loss at this specific frequency is vital from the acoustical point of view. Based on

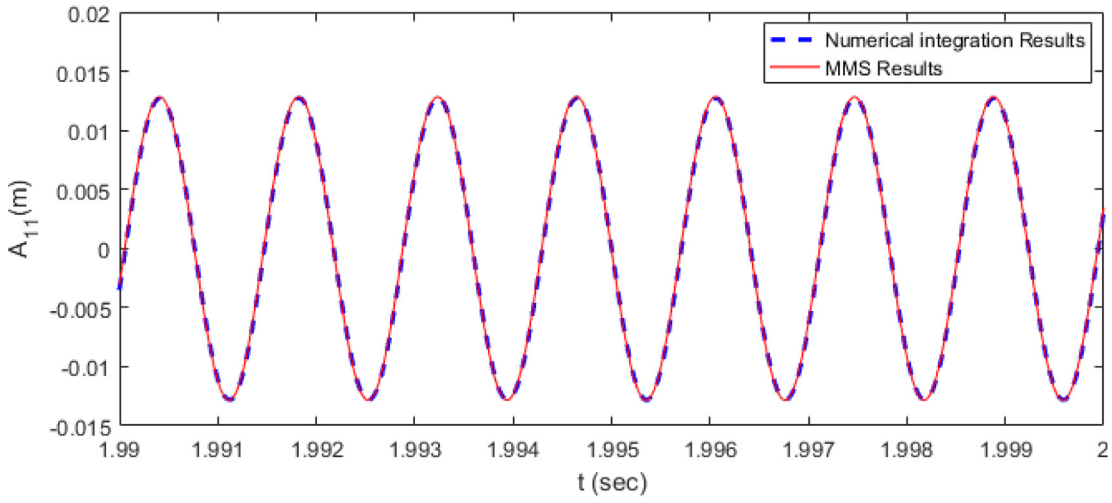

Fig. 3. Comparison of the numerical integration result with the MMS result for the steady state time response of A_{11} about the natural frequency of the linear system (ω_1).

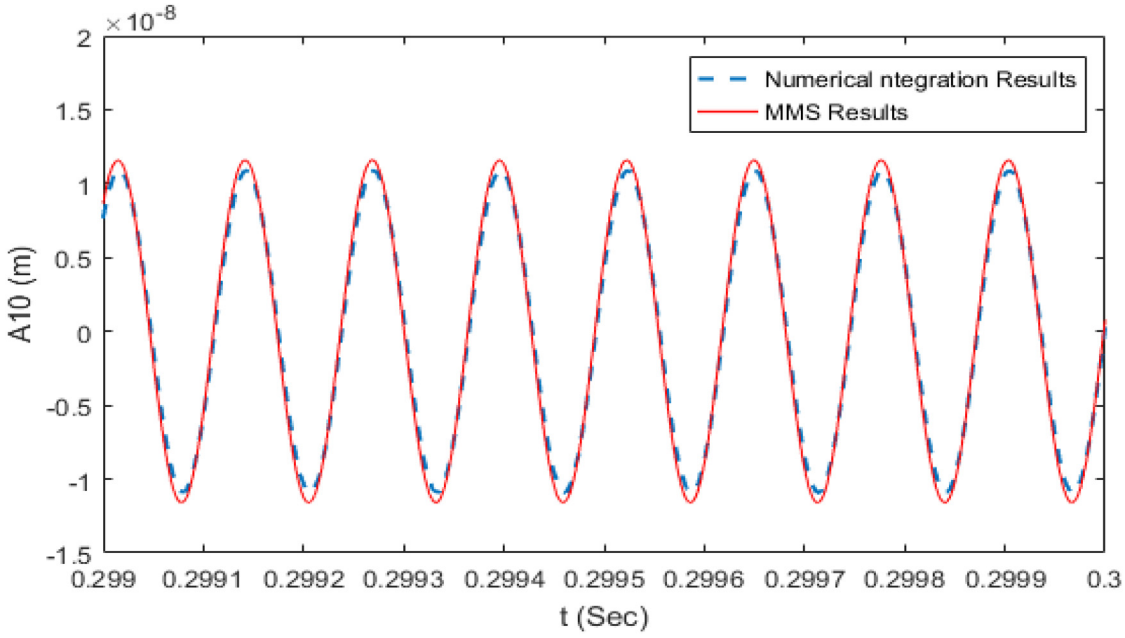

Fig. 4. Comparison of the numerical integration result with the MMS result for the steady state time response of A_{10} about the natural frequency of the linear system (ω_3).

stability analysis Eq. (49) for nonlinear model, the eigenvalues of fixed points are plotted in Fig. 10(c). As shown in this figure, the responses corresponding to the saddle points for $\zeta = 0.001$ and 0.005 are unstable. However for $\zeta = 0.01$, fixed points of the system produce purely real eigenvalues with negative signs. Hence, the responses corresponding to this nodal points are stable. It shows that more probability of occurring jump phenomena exists for the shell with less damping ratio.

Figs. 11(a) and (b) respectively represent the effect of shell thickness on frequency–response and transmission loss of the shell in primary resonance case $\Omega \approx \omega_1$. According to these figures, increasing the shell thickness increases the transmission loss coefficient. For instance, when the thickness is doubled, there is an increase of 17 to 37 dB in the maximum value of the acoustic transmission loss. However, it should be noted that increasing the shell thickness is not always a proper approach to reach better sound insulation ability because of the design restriction in the weight, costs and construction procedure. Hence, this important parameter should be considered along with other design parameters such as length, radius and material properties to achieve the optimal performance in all engineering aspects.

As shown in Fig. 11(b), for the shell with less thickness, minimum transmission loss for the case of increasing the detuning parameter is more than the TL for the case of decreasing the detuning parameter. However for the shell with more thickness, minimum transmission losses for increasing and decreasing the detuning parameter are the same. According to Fig. 11(b), with an increase in the shell thickness from 1 mm to 3 mm, the maximum value of the TL increases about 30% and 120% for the cases of increasing and decreasing detuning parameter, respectively. Fig. 11(c) shows the eigenvalues of fixed points for nonlinear model based on stability analysis Eq. (49). Considering this figure, broader zone of detuning parameter corresponding to singular points with positive real part eigenvalues shows more probability of jump phenomena existence for shell vibration with less shell thickness.

The effects of incident sound amplitude, damping ratio and shell thickness on frequency–response and transmission loss in the primary

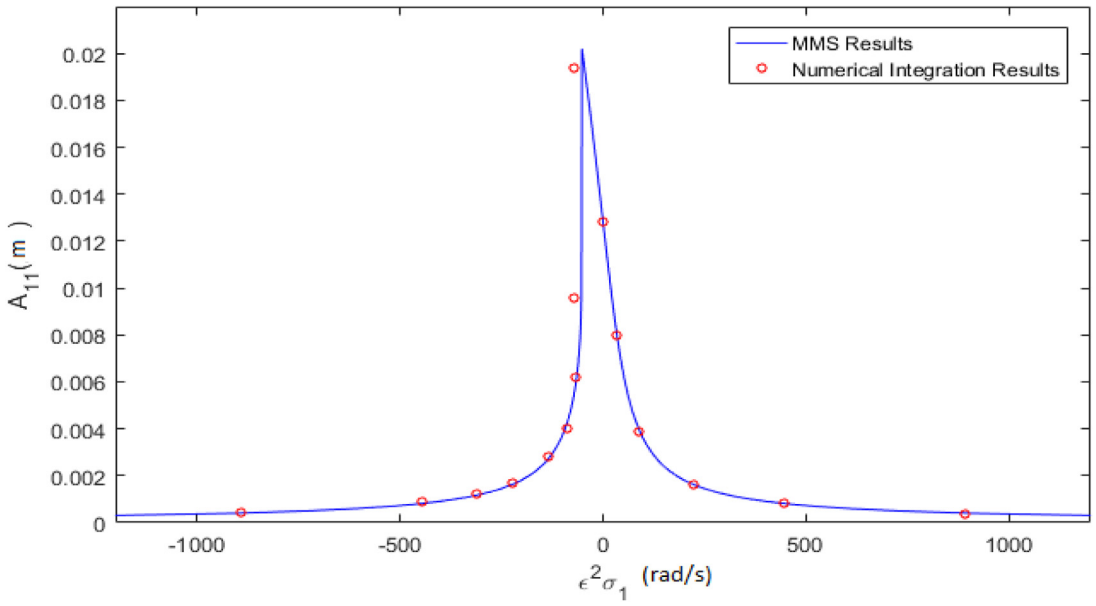

Fig. 5. Comparison of the numerical integration result with the MMS result for the frequency–response of the shell about the natural frequency of the linear system (ω_1).

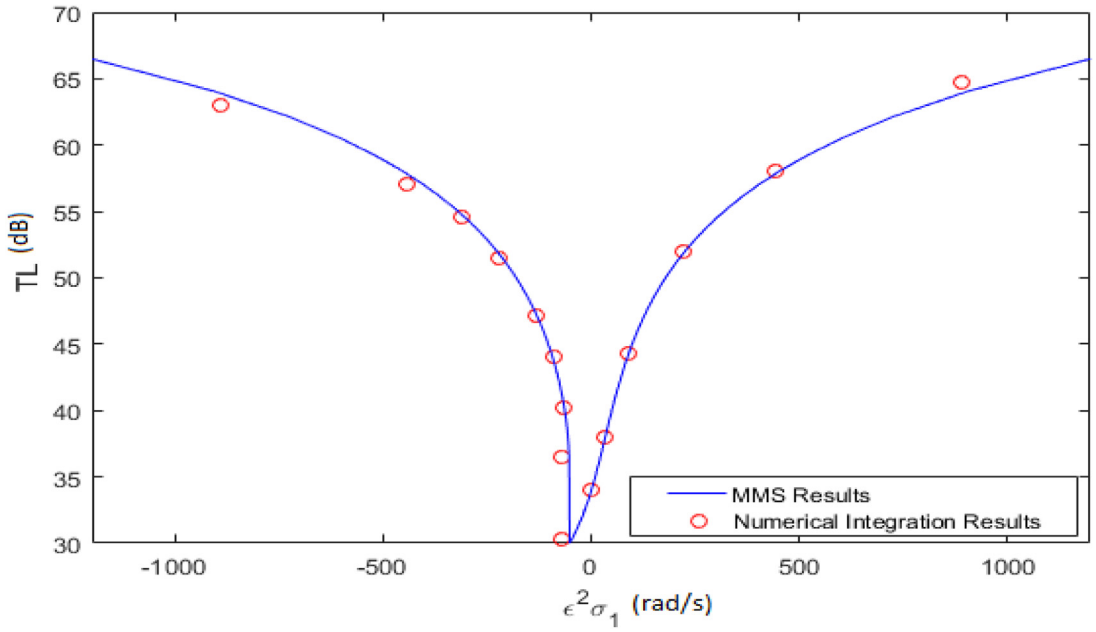

Fig. 6. Comparison of the numerical integration result with the MMS result for the Transmission Loss of the shell about the natural frequency of the linear system (ω_1).

resonance case $\Omega \approx \omega_3$ are investigated and shown in Figs. 12–14. According to these figures, the bending of the curves cannot be seen in this resonance case. Hence, the amplitude of vibration and transmission loss are not changed for increasing and decreasing the detuning parameter about this frequency.

As shown in Fig. 9(b), in the primary resonance case $\Omega \approx \omega_1$ for the case of increasing the detuning parameter, increasing the incident sound level from 190 dB to 200 dB increases the TL from 18 to 24. However according to Fig. 12(b), incident sound level has no significant effect on the transmission loss curve of the cylindrical shell in the primary resonance case $\Omega \approx \omega_3$.

Figs. 13(a) and (b) show the effect of damping ratio on frequency–response and TL in the primary resonance case $\Omega \approx \omega_3$ where $= \frac{c}{(2\rho\omega_3)}$. According to these figures, damping ratio has great effect on frequency–response and TL curves in this resonance case. As shown in Fig. 13(b), with increasing damping ratio from 0.001 to 0.01, the maximum value of the TL increases about 20%.

The effect of shell thickness on frequency–response and transmission loss of the cylindrical shell is investigated in Fig. 14(a) and (b), respectively. Similar to case $\Omega \approx \omega_1$, with an increase in the shell thickness, the transmission loss of the shell increases. According to Fig. 14(b), with increasing the shell thickness from 1 mm to 3 mm, the TL increases about 8%. Hence, the sensitivity of the TL to shell thickness for primary resonance case $\Omega \approx \omega_3$ is less than resonance case $\Omega \approx \omega_1$ when the detuning parameter increases.

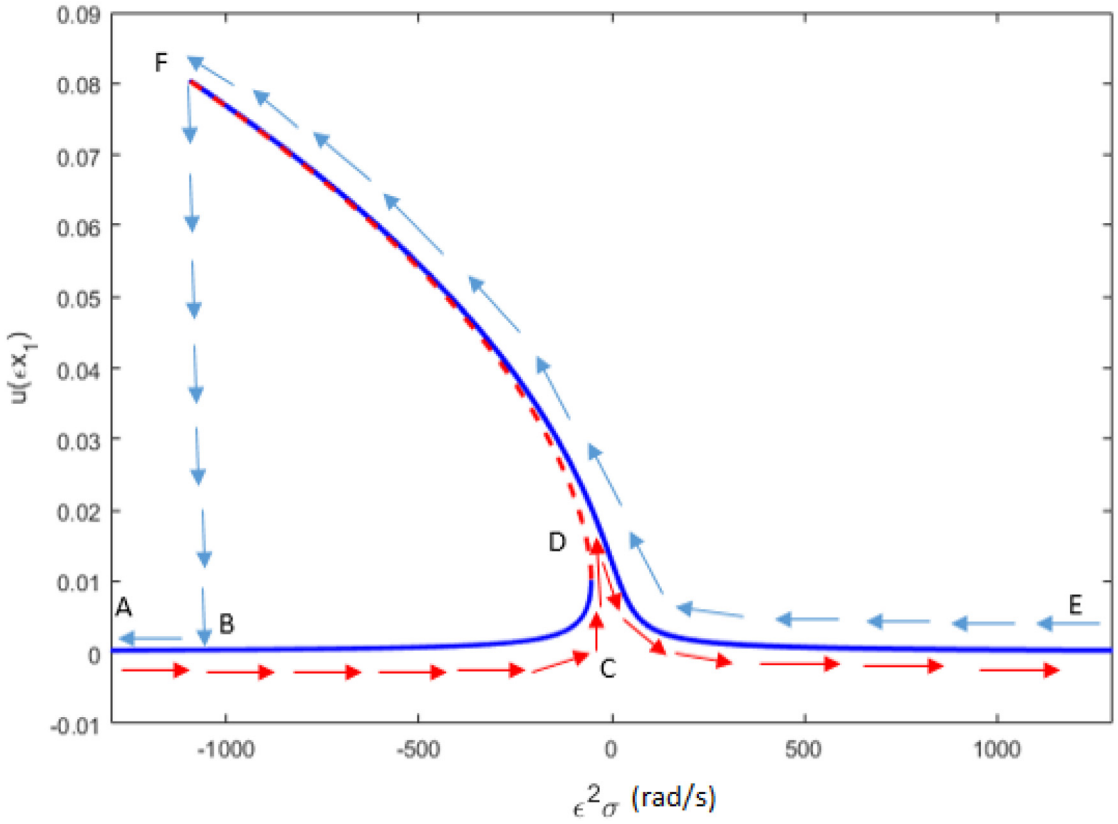

Fig. 7. The frequency–response of the shell about the natural frequency of the linear system (ω_1).

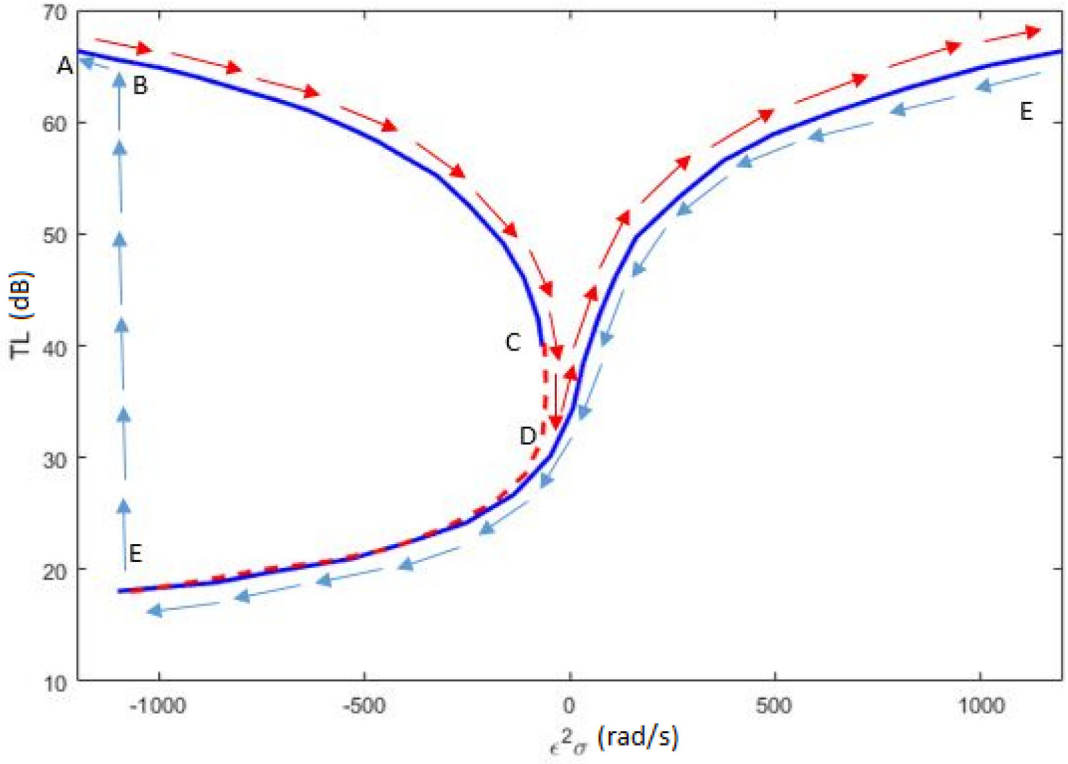

Fig. 8. Transmission Loss of the shell about the natural frequency of the linear system (ω_1).

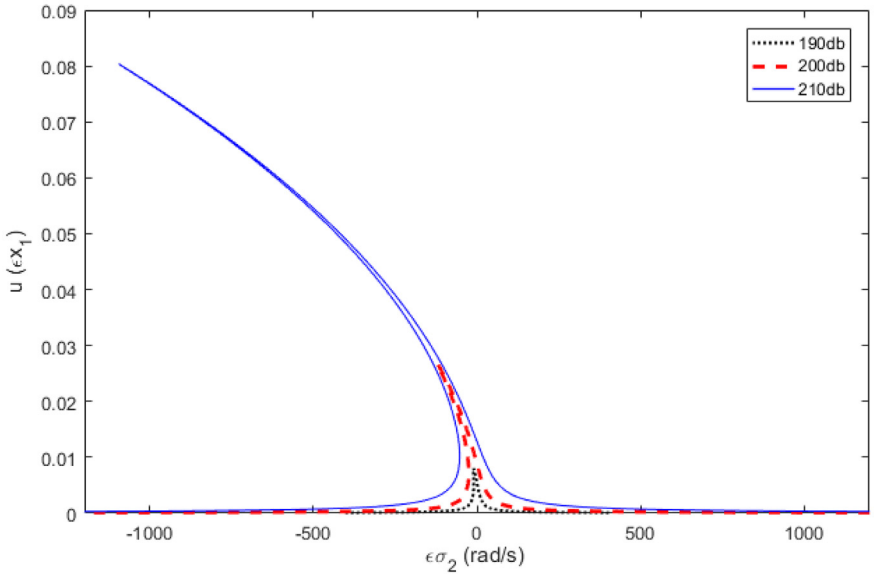

(a)

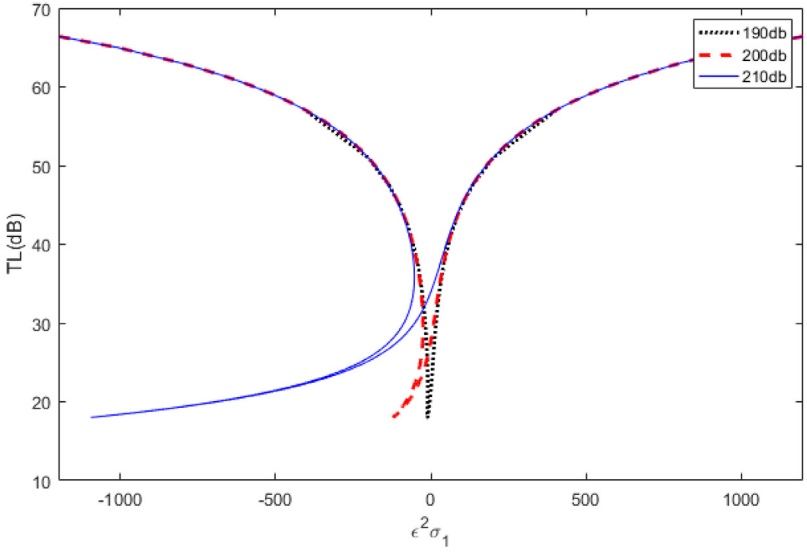

(b)

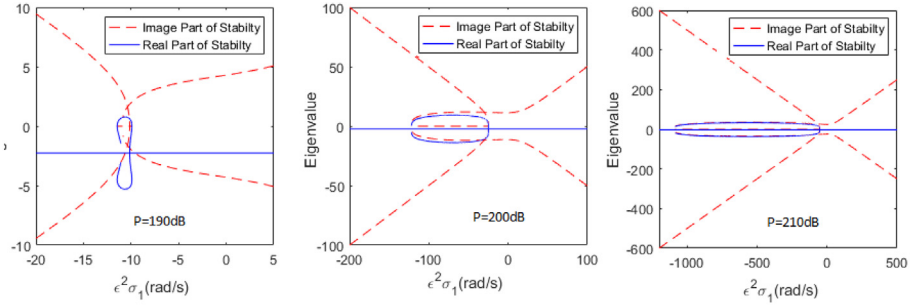

(c)

Fig. 9. The effect of the incident sound amplitude on the frequency–response under the primary resonance condition $\Omega \approx \omega_1$, (a) frequency–response curves, (b) transmission loss curves, (c) stability eigen-values versus detuning parameter.

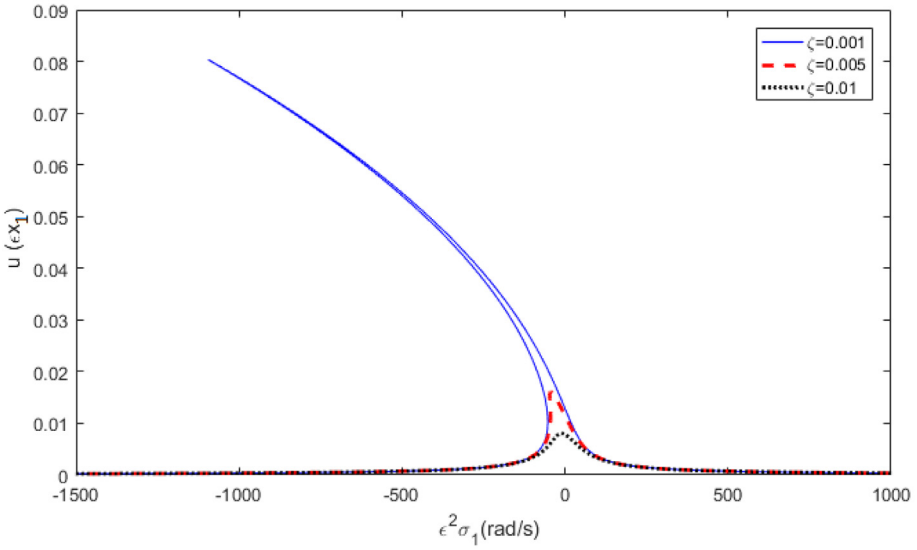

(a)

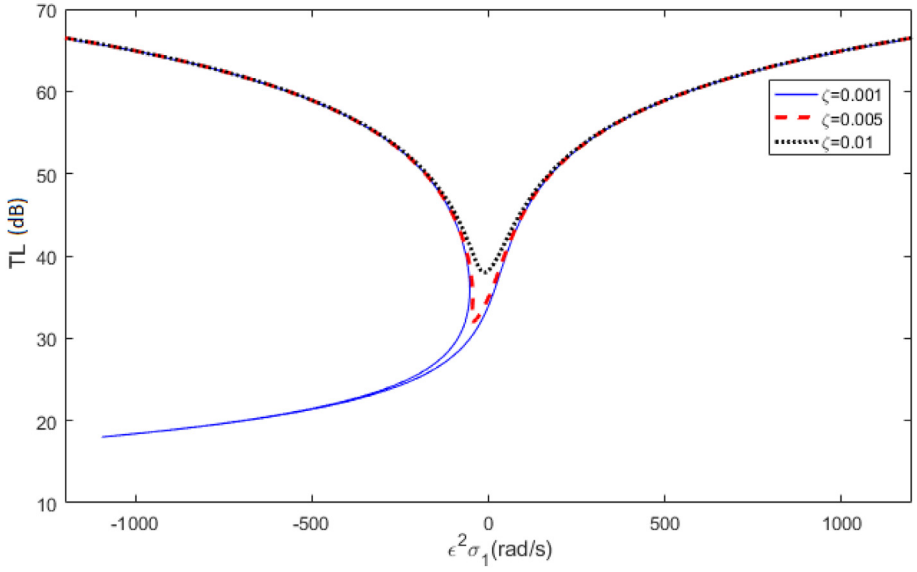

(b)

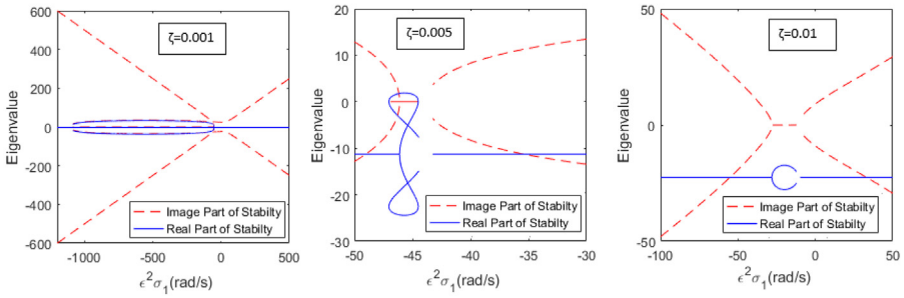

(c)

Fig. 10. The effect of damping ratio on the frequency–response under the primary resonance condition $\Omega \approx \omega_1$, (a) frequency–response curves, (b) transmission loss curves, (c) stability eigen-values versus detuning parameter.

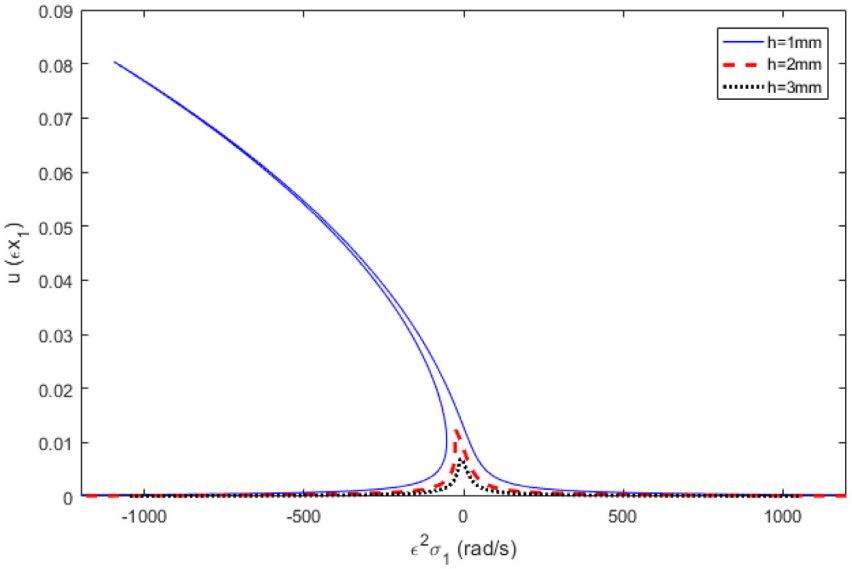

(a)

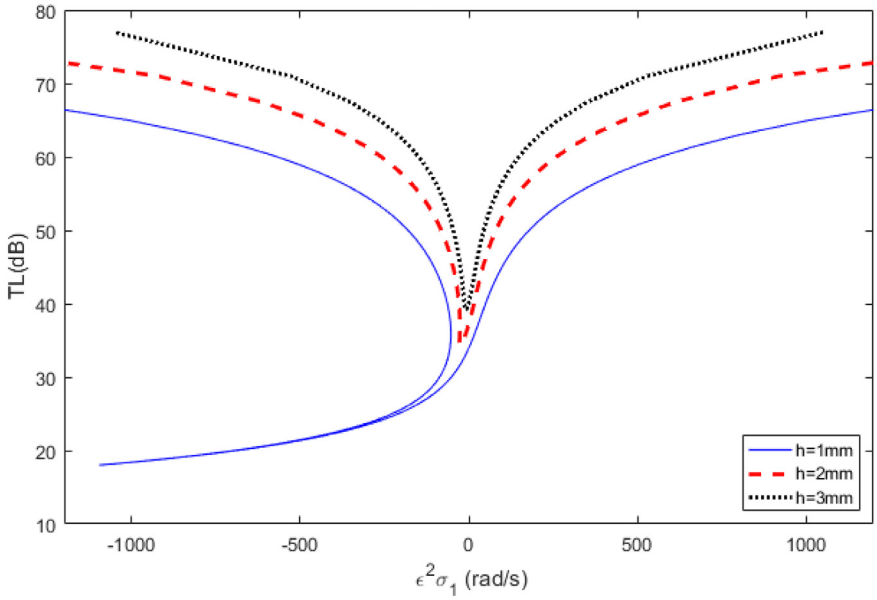

(b)

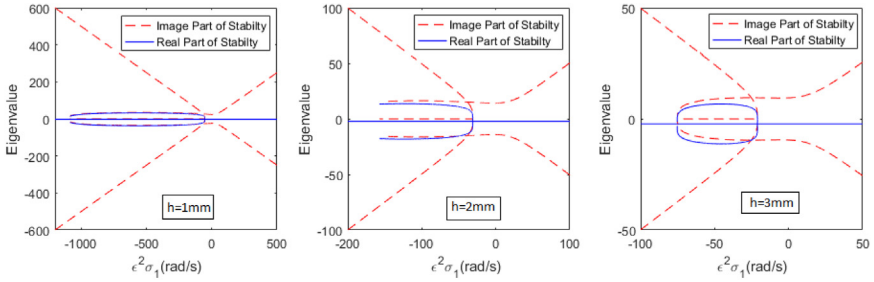

(c)

Fig. 11. The effect of the shell thickness on the frequency–response under the primary resonance condition $\Omega \approx \omega_1$, (a) frequency–response curves, (b) transmission loss curves, (c) stability eigen-values versus detuning parameter.

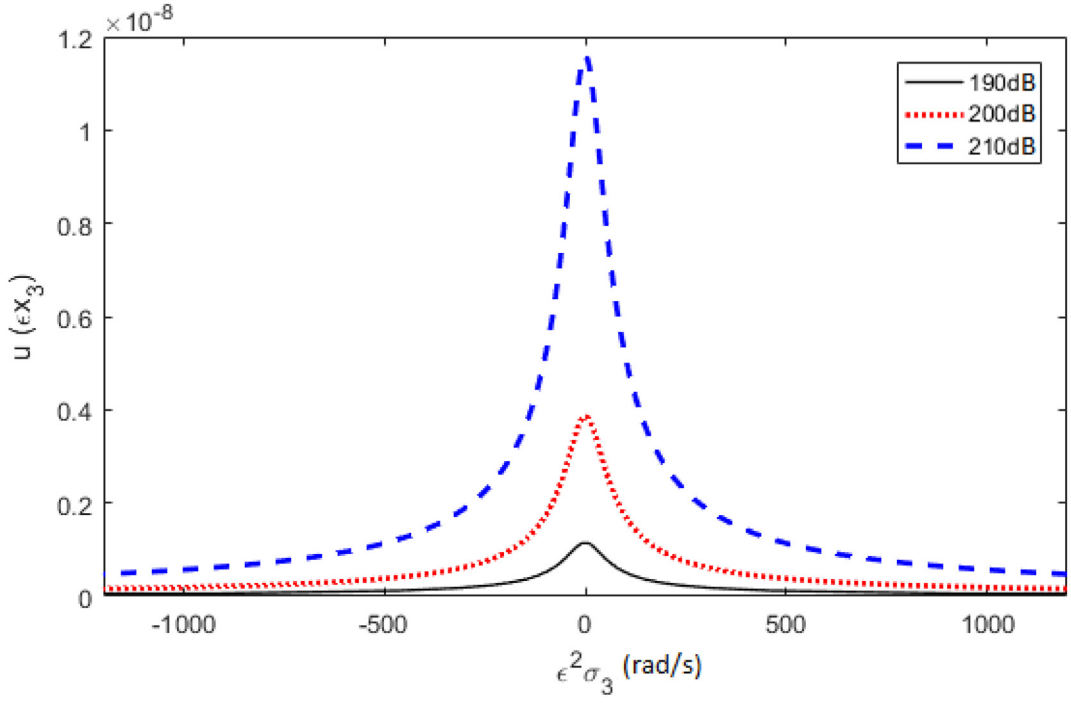

(a)

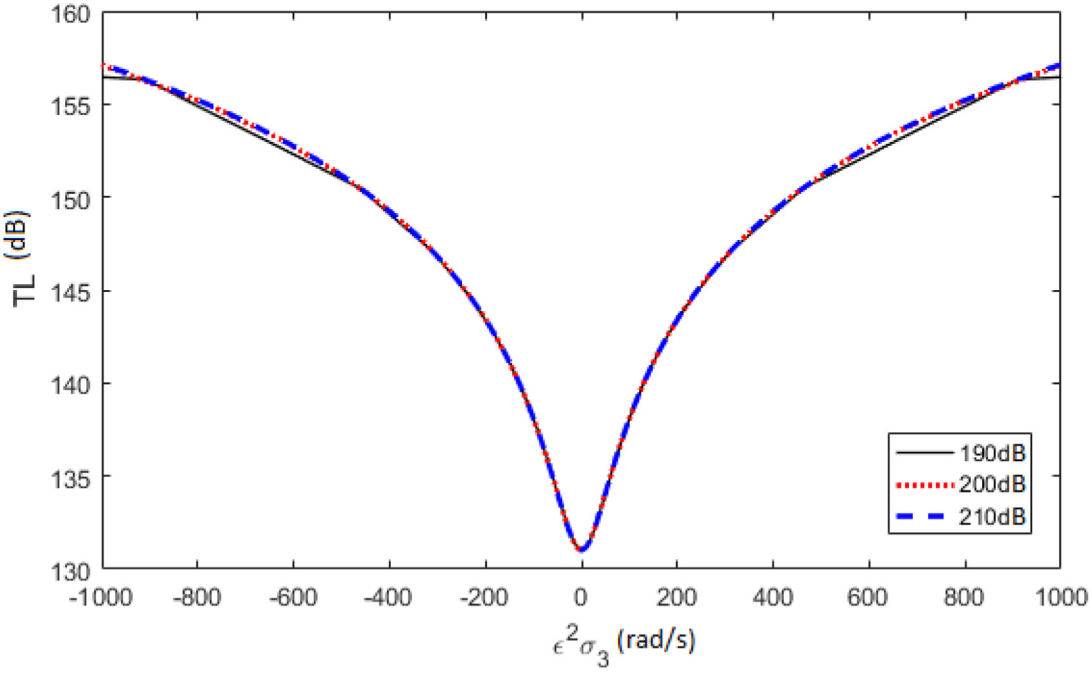

(b)

Fig. 12. The effect of the incident sound amplitude on the frequency–response under the primary resonance condition $\Omega \approx \omega_3$, (a) frequency–response curves, (b) transmission loss curves.

5.2. Bifurcation analysis

The effects of detuning parameter $\epsilon^2\sigma_1$ on the steady-state behavior of the system under primary resonance case ($\Omega \approx \omega_1$) are examined in Figs. 15–17. The simplest way to examine the bifurcation behavior is to select some values of the detuning parameter. Three examples of the steady-state vibration of the cylindrical shell have been calculated based on Eqs. (41) and (29a) and are illustrated in Figs. 15–17. The three examples chosen are $\epsilon^2\sigma_1 = -700$ shown in Fig. 15, $\epsilon^2\sigma_1 = 0$ shown in Fig. 16 and $\epsilon^2\sigma_1 = 200$ shown in Fig. 17. In each example, the upper left-hand diagram presents the phase portrait of steady state response of the system at the selected detuning parameter. Then in the upper right-hand side and in the lower left-hand side, the corresponding steady-state time series of deflection and velocity are shown for each example, respectively. In addition, their Poincare sections are illustrated in the lower right-hand side. As it can be observed, various

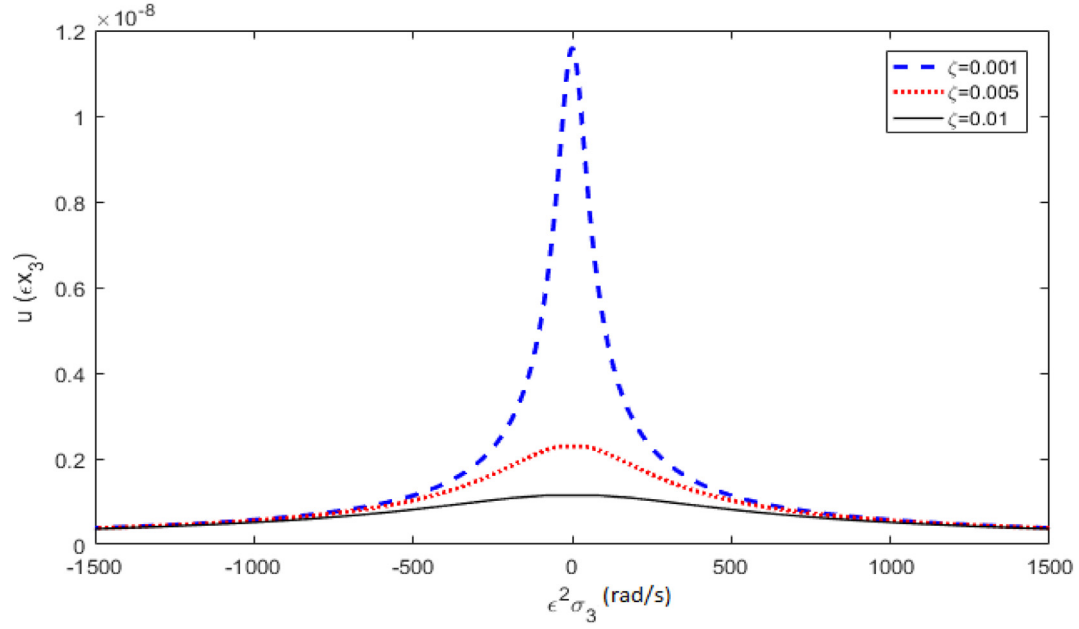

(a)

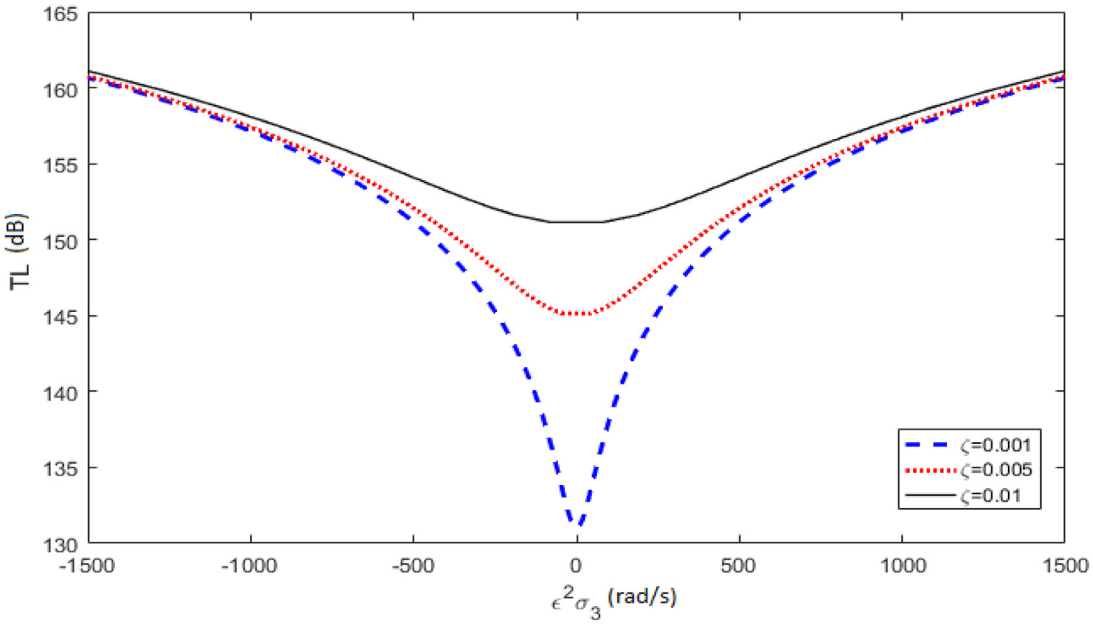

(b)

Fig. 13. The effect of the damping coefficient on the frequency–response under the primary resonance condition $\Omega \approx \omega_3$, (a) frequency–response curves, (b) transmission loss curves.

steady-state dynamic responses can take place over a relatively short detuning parameter range due to the effect of the nonlinearity. In addition, as detuning parameter is varied, some changes occur in the shell steady-state dynamic behavior. These qualitative changes in the shell dynamic behavior are so-called bifurcation phenomena, and the detuning parameter is called a bifurcation parameter.

In Fig. 15, a bifurcation phenomenon of period-3 motion at $\epsilon^2\sigma_1 = -700$ is investigated. Period-1 orbit at $\epsilon^2\sigma_1 = 0$ and its Poincare section, displacement response, and velocity-time diagram are illustrated in Fig. 16. Finally, Fig. 17 shows the Neimark–Sacker bifurcation behavior of the shell oscillations at $\epsilon^2\sigma_1 = 200$ [29].

In Fig. 18, the bifurcation diagram of Poincare maps is presented for variations in the detuning parameter. In this diagram, the results show the value of the A_{11} parameter when its velocity is zero. As it can be seen in this figure, different kinds of the shell dynamic behavior occur by variation of the detuning parameter. It is also possible to observe well-known bifurcations such as flip and Neimark–Sacker in this figure.

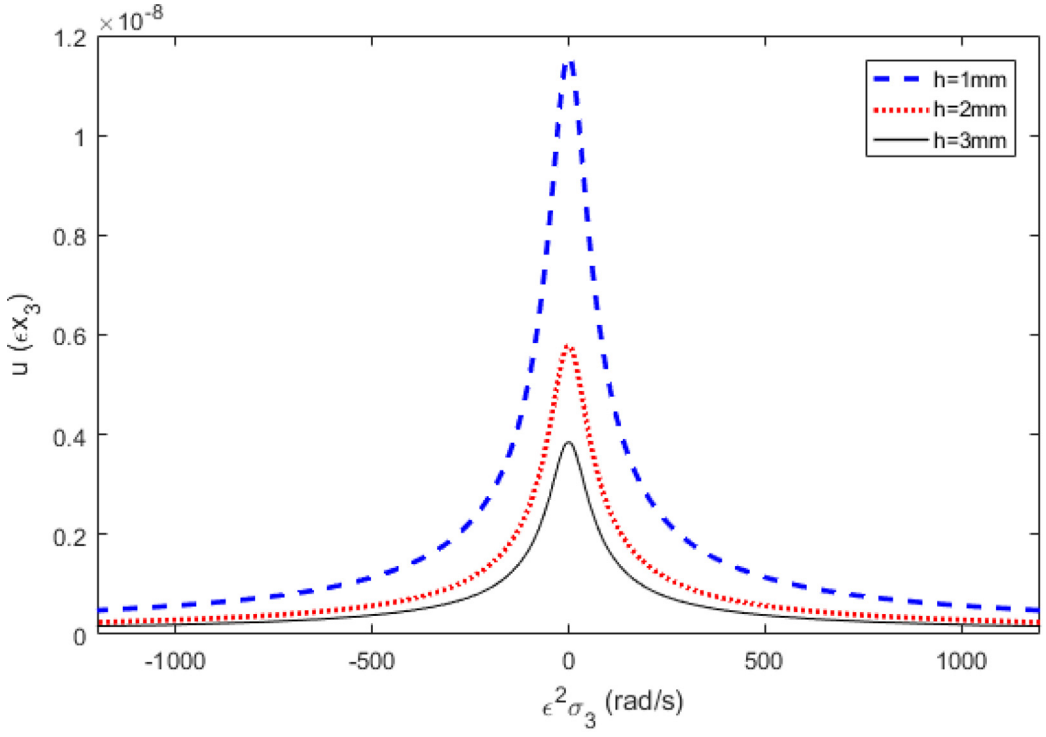

(a)

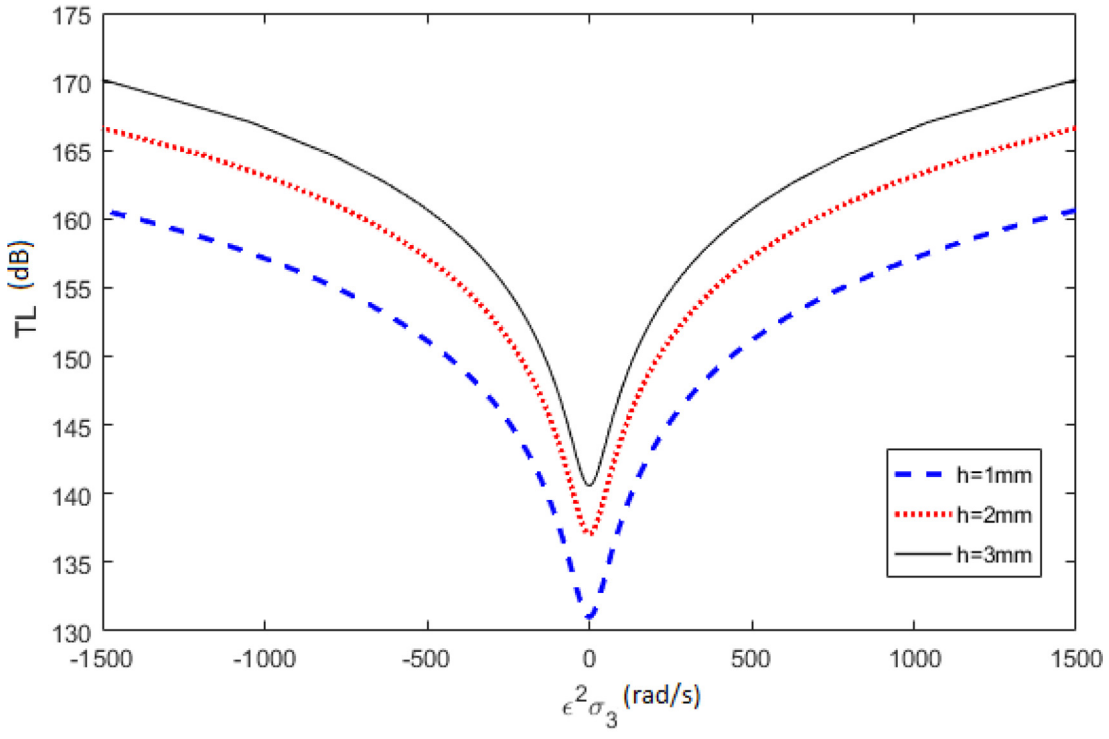

(b)

Fig. 14. The effect of the shell thickness on the frequency–response under the primary resonance condition $\Omega \approx \omega_3$, (a) frequency–response curves, (b) transmission loss curves.

6. Conclusion

Vibro-acoustic behavior of cylindrical shell under primary resonances was analytically studied in this paper. Donnell's nonlinear shallow shell theory was used to derive the partial differential equations of the shell radial motion. Then, the Galerkin method was employed to achieve the coupled nonlinear ordinary differential equations of the system. Also, in order to solve the nonlinear equations of system, Multiple Scales method was used. Closed-form expressions were obtained for the amplitude of vibration and transmission loss versus the frequency

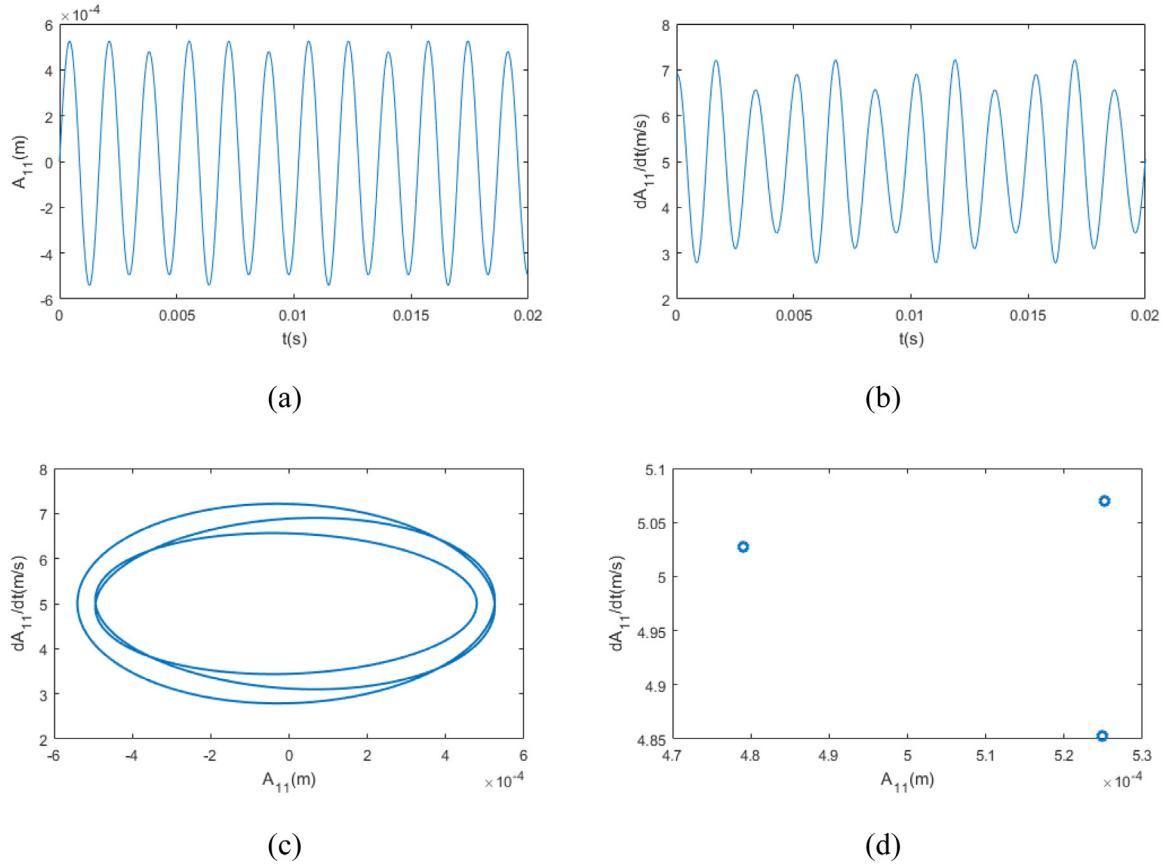

Fig. 15. Period-3 bifurcation: The steady-state dynamic behavior of the system including (a) the time series of displacement, (b) the time series of velocity, (c) the phase portrait, (d) the Poincare section for $\epsilon^2\sigma_1 = -700$ under primary resonances condition.

of the incident wave in different primary resonance conditions $\Omega \approx \omega_1$ and $\Omega \approx \omega_3$. According to the obtained results, following remarks can be made:

1- Unlike the primary resonance about $\Omega \approx \omega_3$, for the case of primary resonance ($\Omega \approx \omega_1$), jump phenomenon can be seen in frequency–response of shell vibration and transmission loss curve.
2- For the case of primary resonance ($\Omega \approx \omega_1$), increasing the amplitude of the incident wave increases the minimum value of the transmission loss through the shell in the case of increasing the detuning parameter. However, in the case of decreasing the detuning parameter, the amplitude of the incident wave does not affect the minimum transmission loss through the cylindrical shell.
3- Incident sound level has no significant effect on the transmission loss curve of the cylindrical shell in the primary resonance case $\Omega \approx \omega_3$.
4- With increasing the shell thickness from 1 mm to 3 mm, a significant improvement could be observed in the value of TL up to 120 percent about resonance frequency $\Omega \approx \omega_3$.
5- Increasing the damping ratio from 0.001 to 0.01 increases the maximum value of the transmission loss up to 20% and 111% around the resonance frequencies ω_1 and ω_3, respectively. Therefore, using materials with more damping coefficient turned out to improve acoustical behavior of the cylindrical shell around these resonance frequencies.
6- Under primary resonance case $\Omega \approx \omega_1$, varying the detuning parameter can change the limit cycle behavior of the steady-state response of the cylindrical shell. It means that the detuning parameter is a bifurcation parameter.

CRediT authorship contribution statement

Amir Hossein Orafa: Conceptualization, Methodology, Software, Validation, Formal analysis. **Mohammad Mahdi Jalili:** Conceptualization, Investigation, Data curation, Writing - original draft. **Ali Reza Fotuhi:** Writing - review & editing.

Declaration of competing interest

The authors declare that they have no known competing financial interests or personal relationships that could have appeared to influence the work reported in this paper.

Appendix A

Coefficients of Eq. (6):

$$c_1(t) = -\frac{3EhR^2{\lambda_1}^2}{2n^2} A_{10}(t)\, A_{1n}(t)$$

$$c_2(t) = -\frac{3EhR^2{\lambda_1}^2}{2n^2} A_{10}(t)\, B_{1n}(t)$$

$$c_3 = \frac{3Eh}{{\lambda_1}^2 R} A_{10}(t)$$

$$c_4 = \frac{Eh{\lambda_1}^2}{R({\lambda_1}^2 + \left(\frac{n}{R}\right)^2)^2} A_{1n}(t)$$

$$c_5(t) = \frac{Eh{\lambda_1}^2}{R({\lambda_1}^2 + \left(\frac{n}{R}\right)^2)^2} B_{1n}(t)$$

$$c_6(t) = \frac{Ehn^2(A_{1n}(t)^2 + B_{1n}(t)^2)}{32{\lambda_1}^2 R^2}$$

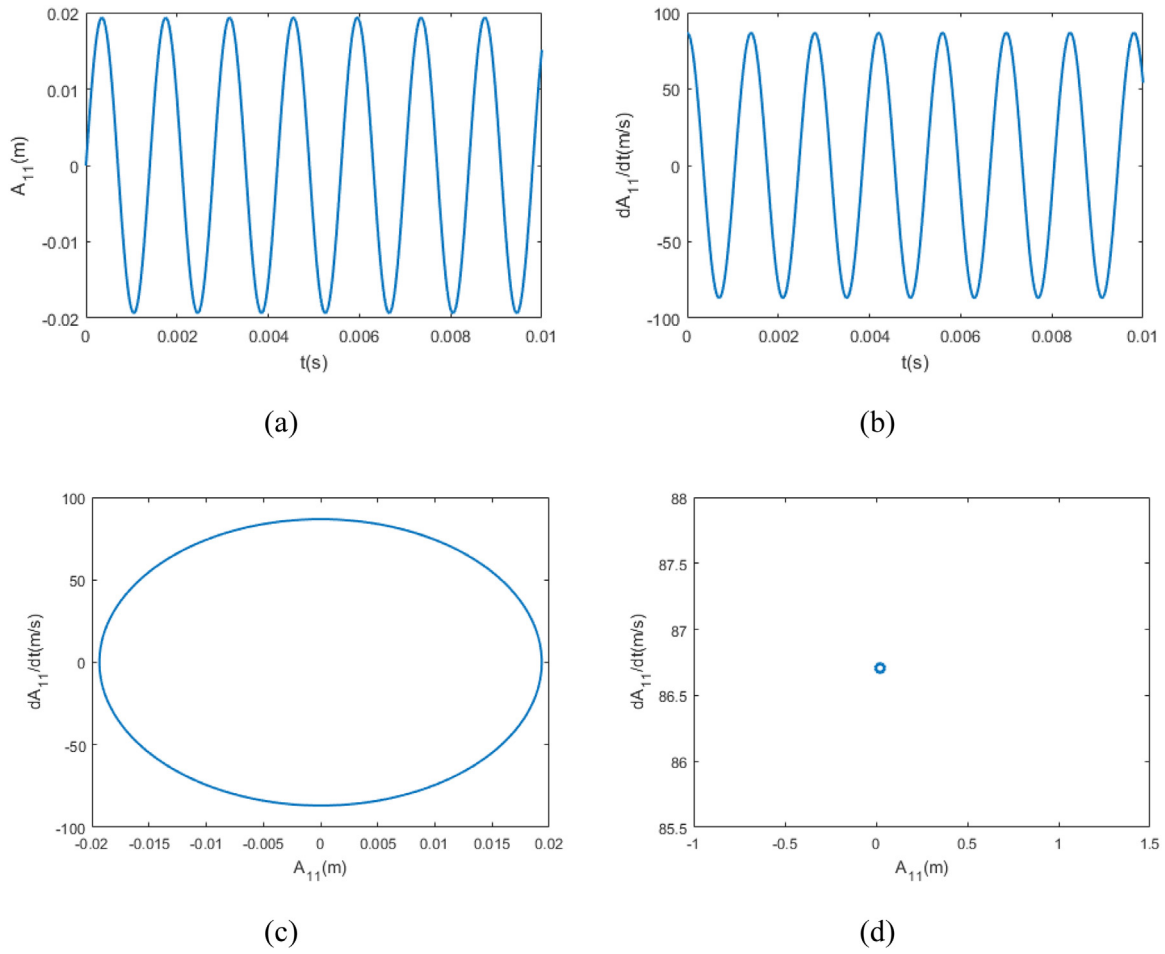

Fig. 16. Period-1 orbit: The steady-state dynamic behavior of the system including (a) the time series of displacement, (b) the time series of velocity, (c) the phase portrait, (d) the Poincare section for $\epsilon^2\sigma_1 = 0$ under primary resonances condition.

$$
\begin{aligned}
c_7(t) &= \frac{EhR^2{\lambda_1}^2(-A_{1n}(t)^2 + B_{1n}(t)^2)}{32n^2}\\
c_8(t) &= -\frac{EhR^2{\lambda_1}^2}{16n^2}A_{1n}(t)\,B_{1n}(t)\\
c_9(t) &= \frac{12Ehn^2{\lambda_1}^2}{2R^2(4{\lambda_1}^2 + \left(\frac{n}{R}\right)^2)^2}A_{10}(t)\,A_{1n}(t)\\
c_{10}(t) &= \frac{12Ehn^2{\lambda_1}^2}{2R^2(4{\lambda_1}^2 + \left(\frac{n}{R}\right)^2)^2}A_{10}(t)\,B_{1n}(t)\\
c_{11}(t) &= -\frac{Eh}{9{\lambda_1}^2R}A_{10}(t)\\
c_{12}(t) &= -\frac{9Ehn^2{\lambda_1}^2}{2R^2(16{\lambda_1}^2 + \left(\frac{n}{R}\right)^2)^2}A_{10}(t)\,A_{1n}(t)\\
c_{13}(t) &= -\frac{9Ehn^2{\lambda_1}^2}{2R^2(16{\lambda_1}^2 + \left(\frac{n}{R}\right)^2)^2}A_{10}(t)\,B_{1n}(t)
\end{aligned}
\tag{A.1}
$$

Appendix B

Coefficients of Eqs. (21) to (23)

$$
\begin{aligned}
P_1 &= \frac{D\left({\lambda_1}^2 + \frac{n^2}{R^2}\right)^2 - \frac{\pi L}{2}h_4}{(\rho h - Re\,(G_4))}\\
P_2 &= -\frac{h}{\rho h - Re\,(G_4)}\\
P_3 &= \frac{2h_1}{\pi L\,(\rho h - Re\,(G_4))}\\
P_4 &= \frac{2h_2}{\pi L\,(\rho h - Re\,(G_4))}\\
P_5 &= \frac{2h_3}{\pi L\,(\rho h - Re\,(G_4))}\\
P_6 &= \frac{2G_8}{\pi L\,(\rho h - Re\,(G_4))}\\
\varnothing_1 &= (\frac{G_3}{G_2})
\end{aligned}
\tag{B.1}
$$

$$
\begin{aligned}
Q_1 &= \frac{D\left({\lambda_1}^2 + \frac{n^2}{R^2}\right)^2 - \frac{\pi L}{2}h_4}{\rho h}\\
Q_2 &= -\frac{1}{\rho}\\
Q_3 &= \frac{2h_1}{\pi L\rho h}\\
Q_4 &= \frac{2h_2}{\pi L\rho h}\\
Q_5 &= \frac{2h_3}{\pi L\rho h}
\end{aligned}
\tag{B.2}
$$

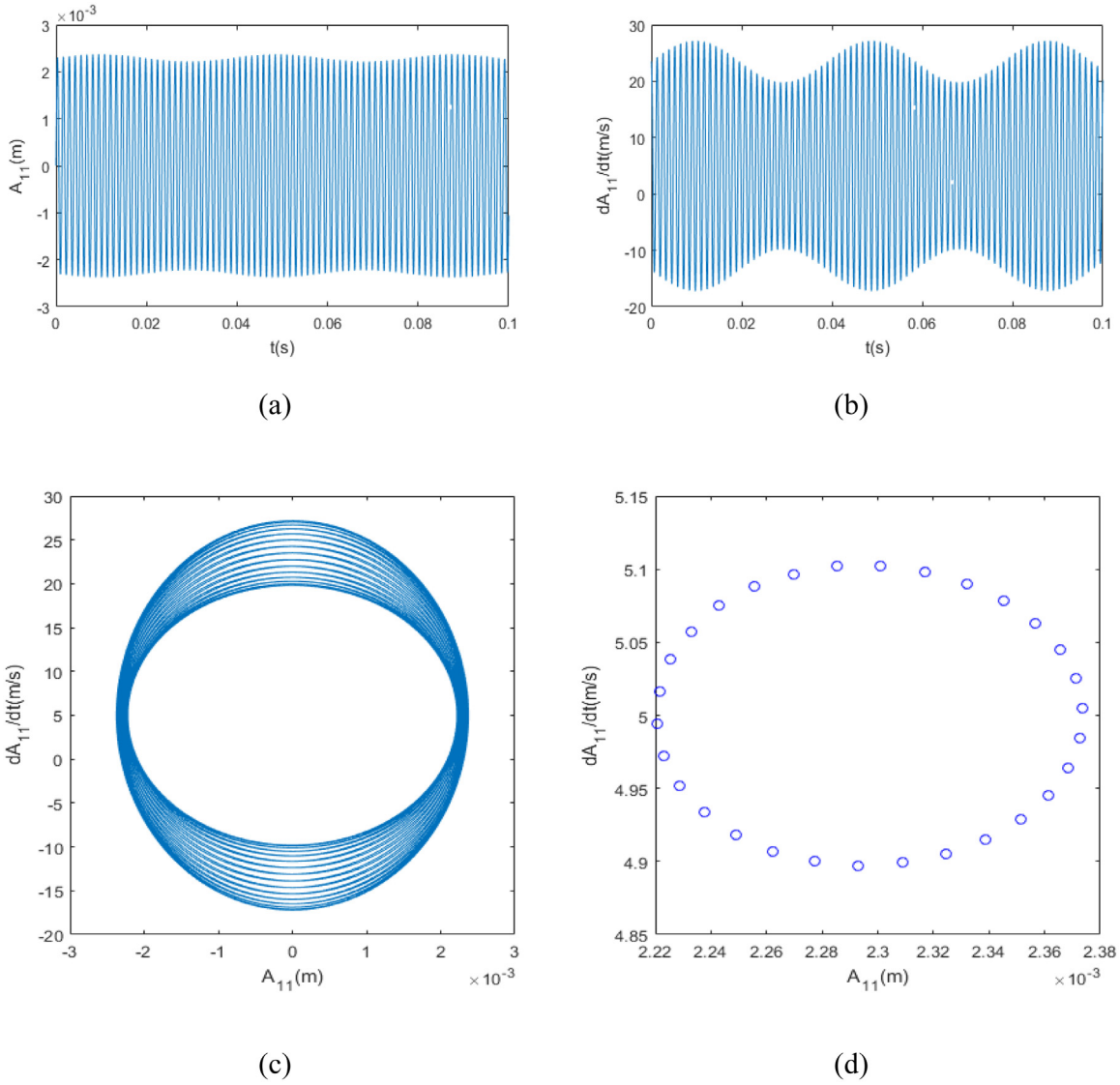

Fig. 17. Neimark–Sacker bifurcation: The steady-state dynamic behavior of the system including (a) the time series of displacement, (b) the time series of velocity, (c) the phase portrait, (d) the Poincare section for $\epsilon^2\sigma_1 = 200$ under primary resonances condition.

$$
\begin{aligned}
\Pi_1 &= \frac{90D{\lambda_1}^4\pi L - k_5}{10\pi L\left(\rho h - Re\left(G_7\right)\right)}\\
\Pi_2 &= -\frac{h}{\rho h - Re\left(G_7\right)}\\
\Pi_3 &= \frac{k_1}{10\pi L\left(\rho h - Re\left(G_7\right)\right)}\\
\Pi_4 &= \frac{k_2}{10\pi L\left(\rho h - Re\left(G_7\right)\right)}\\
\Pi_6 &= \frac{G_9}{10\pi L\left(\rho h - Re\left(G_7\right)\right)}\\
\varnothing_2 &= \left(\frac{G_6}{G_5}\right)
\end{aligned}
\tag{B.3}
$$

where

$$
\begin{aligned}
G_2 &= real\left\{2P_0(-j)^n\left(J_n\left(K_{1r}r\right) - \frac{J_n'\left(K_{1r}r\right)H_n^2\left(K_{1r}r\right)}{H_n^{2\prime}\left(K_{1r}r\right)}\right)\right.\\
&\quad\left.\times\ \frac{L\pi^2\left(1+e^{-jK_{1x}L}\right)}{\pi^2 - L^2K_{1x}^2}\right\}\\
G_3 &= image\left\{2P_0(-j)^n\left(J_n\left(K_{1r}r\right) - \frac{J_n'\left(K_{1r}r\right)H_n^2\left(K_{1r}r\right)}{H_n^{2\prime}\left(K_{1r}r\right)}\right)\right.\\
&\quad\left.\times\ \frac{L\pi^2\left(1+e^{-jK_{1x}L}\right)}{\pi^2 - L^2K_{1x}^2}\right\}\\
G_4 &= \left(\rho_3\frac{H_n^1\left(K_{3r}r\right)}{H_n^{1\prime}\left(K_{3r}r\right)} - \rho_1\frac{H_n^2\left(K_{1r}r\right)}{H_n^{2\prime}\left(K_{1r}r\right)}\right)\\
G_5 &= real\left\{P_0\left(J_0\left(K_{1r}r\right) - \frac{J_0'\left(K_{1r}r\right)H_0^2\left(K_{1r}r\right)}{H_0^{2\prime}\left(K_{1r}r\right)}\right)\right.\\
&\quad\left.\times\left(\frac{-1}{9\pi^2 - L^2K_{1x}^2} + \frac{1}{\pi^2 - L^2K_{1x}^2}\right)6L\pi^2\left(1+e^{-jK_{1x}L}\right)\right\}\\
G_6 &= image\left\{P_0\left(J_0\left(K_{1r}r\right) - \frac{J_0'\left(K_{1r}r\right)H_0^2\left(K_{1r}r\right)}{H_0^{2\prime}\left(K_{1r}r\right)}\right)\right.\\
&\quad\left.\times\left(\frac{-1}{9\pi^2 - L^2K_{1x}^2} + \frac{1}{\pi^2 - L^2K_{1x}^2}\right)6L\pi^2\left(1+e^{-jK_{1x}L}\right)\right\}\\
G_7 &= \left(\rho_3\frac{H_0^1\left(K_{3r}r\right)}{H_0^{1\prime}\left(K_{3r}r\right)} - \rho_1\frac{H_0^2\left(K_{1r}r\right)}{H_0^{2\prime}\left(K_{1r}r\right)}\right)
\end{aligned}
\tag{B.4}
$$

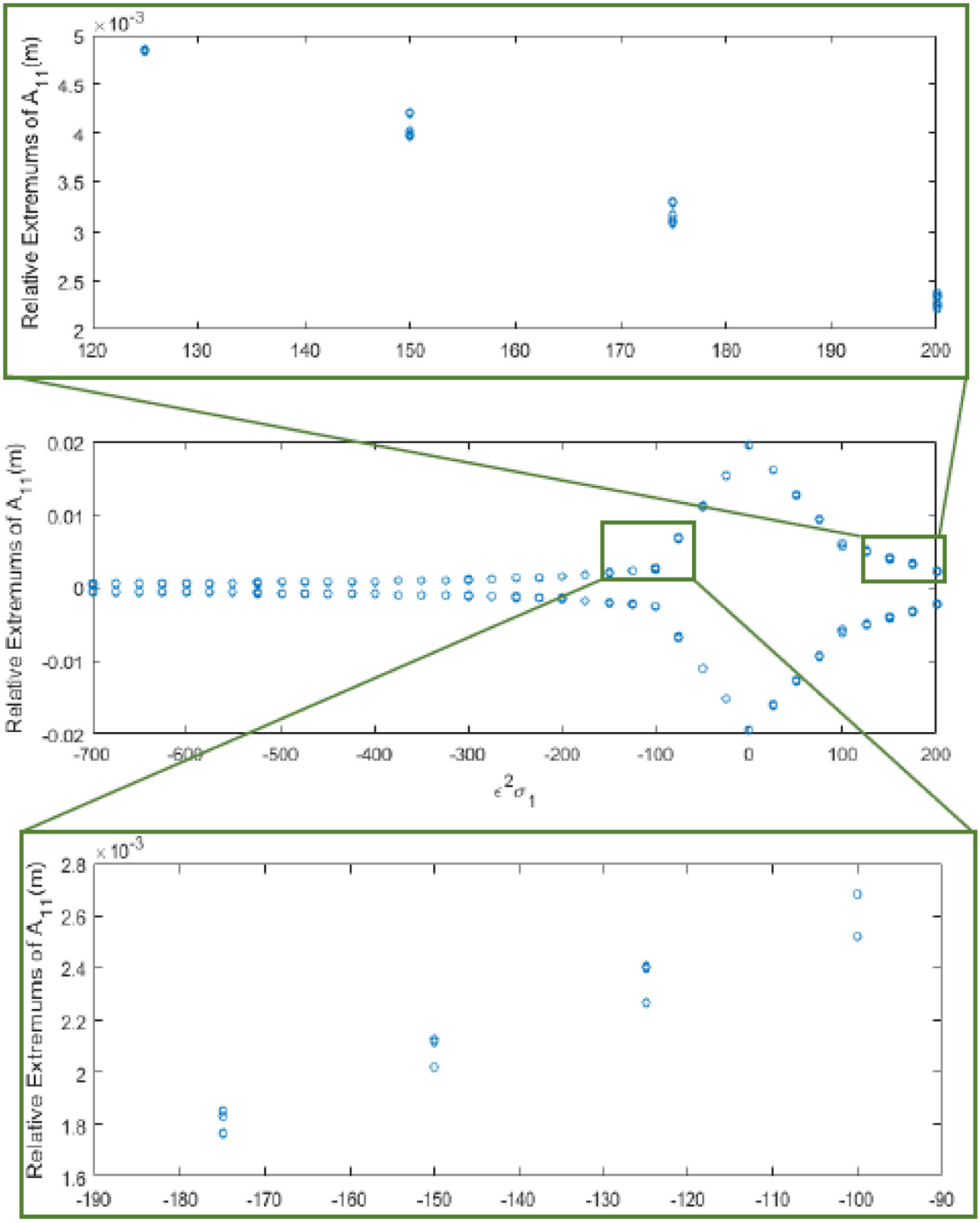

Fig. 18. Bifurcation diagram of Poincaré maps of the shell vibration with increasing detuning parameter.

$$G_8 = \sqrt{{G_2}^2 + {G_3}^2}$$

$$G_9 = \sqrt{{G_6}^2 + {G_5}^2}$$

References

[1] K. Daneshjou, R. Talebitooti, A. Tarkashv, Analysis of sound transmission loss through thick-walled cylindrical shell using three-dimensional elasticity theory, Int. J. Mech. Sci. 106 (2016) 286–296.

[2] P. Oliazadeh, A. Farshidianfar, Analysis of different techniques to improve sound transmission loss in cylindrical shells, J. Sound Vib. 389 (2017) 276–291.

[3] Q. Zhang, Y. Mao, D. Qi, Effect of perforation on the sound transmission through a double-walled cylindrical shell, J. Sound Vib. 410 (2017) 344–363.

[4] P. Oliazadeh, A. Farshidianfar, M.J. Crocker, Experimental and analytical investigation on sound transmission loss of cylindrical shells with absorbing material, J. Sound Vib. 434 (2018) 28–43.

[5] X. Wang, E. Xu, C. Jiang, W. Wu, Vibro-acoustic behavior of double-walled cylindrical shells with general boundary conditions, Ocean Eng. 192 (2019) 1–10.

[6] M.J. Kingan, Y. Yang, B.R. Mace, Sound transmission through cylindrical structures using a wave and finite element method, Wave Motion 87 (2019) 58–74.

[7] J. Magniez, J.D. Chazot, M.A. Hamdi, B. Troclet, A mixed 3D-shell analytical model for the prediction of sound transmission through sandwich cylinders, J. Sound Vib. 333 (2014) 4750–4770.

[8] R. Talebitooti, K. Daneshjou, A. Tarkashv, Study of imperfect bonding effects on sound transmission loss through functionally graded laminated sandwich cylindrical shells, Int. J. Mech. Sci. 133 (2017) 469–483.

[9] R. Talebitooti, M.R. Zarastv, M.R. Gheibi, Acoustic transmission through laminated composite cylindrical shell employing third order shear deformation theory in the presence of subsonic flow, Compos. Struct. 157 (2016) 95–110.
[10] V. Rabbani, M. Hodaei, X. Deng, H. Lu, D. Hui, N. Wu, Sound transmission through a thick-walled FGM piezo-laminated cylindrical shell filled with and submerged in compressible fluids, J. Sound Vib. 197 (2019) 1–18.
[11] J. Zhou, A. Bhaskar, X. Zhang, The effect of external mean flow on sound transmission through double-walled cylindrical shells lined with poroelastic material, J. Sound Vib. 333 (2014) 1972–1990.
[12] J. Zhou, A. Bhaskar, X. Zhang, Sound transmission through double cylindrical shells lined with porous material under turbulent boundary layer excitation, J. Sound Vib. 357 (2015) 253–268.
[13] Y. Liu, C. He, Diffuse field sound transmission through sandwich composite cylindrical shells with poroelastic core and external mean flow, Compos. Struct. 135 (2016) 383–396.
[14] J. Magniez, M.A. Hamdi, J.D. Chazot, B. Troclet, A mixed Biot–shell analytical model for the prediction of sound transmission through a sandwich cylinder with a poroelastic core, J. Sound Vib. 360 (2016) 203–223.
[15] R. Talebitooti, K. Daneshjou, M. Kornokar, Three dimensional sound transmission through poroelastic cylindrical shells in the presence of subsonic flow, J. Sound Vib. 363 (2016) 380–406.
[16] R. Talebitooti, K. Daneshjou, M. Kornokar, Three dimensional sound transmission through poroelastic cylindrical shells in the presence of subsonic flow, J. Sound Vib. 363 (2016) 380–406.
[17] R. Talebitooti, H.D. Gohari, M.R. Zarastv, Multi objective optimization of sound transmission across laminated composite cylindrical shell lined with porous core investigating non-dominated sorting genetic algorithm, Aerosp. Sci. Technol. 69 (2017) 269–280.
[18] F. Pellicano, M. Amabili, M.P. Païdoussis, Effect of the geometry on the nonlinear vibration of circular cylindrical shells, Int. J. Nonlinear Mech. 37 (2002) 1181–1198.
[19] M. Amabili, A comparison of shell theories for large-amplitude vibrations of circular cylindrical shells: Lagrangian approach, J. Sound Vib. 264 (2003) 1091–1125.
[20] K.N. Karagiozis, M. Amabili, M.P. Païdoussis, A.K. Misra, Nonlinear vibrations of fluid-filled clamped circular cylindrical shells, J. Fluids Struct. 21 (2005) 579–595.
[21] M. Amabili, K. Karagiozis, M.P. Païdoussis, Effect of geometric imperfections on non-linear stability of circular cylindrical shells conveying fluid, Int. J. Nonlinear Mech. 44 (2010) 276–289.
[22] Ye Kurylov, M. Amabili, Polynomial versus trigonometric expansions for nonlinear vibrations of circular cylindrical shells with different boundary conditions, J. Sound Vib. 329 (2010) 1435–1449.
[23] F. Alijani, M. Amabili, Nonlinear vibrations and multiple resonances of fluid filled arbitrary laminated circular cylindrical shells, Compos. Struct. 108 (2014) 951–962.
[24] M. Amabili, P. Balasubramanian, G. Ferrari, Travelling wave and non-stationary response in nonlinear vibrations of water-filled circular cylindrical shells: Experiments and simulations, J. Sound Vib. 381 (2016) 220–245.
[25] A. Yadav, M. Amabili, S.K. Panda, T. Dey, R. Kumar, Nonlinear damped vibrations of three-phase CNT-FRC circular cylindrical shell, Compos. Struct. 255 (2021) 951–962.
[26] M. Sadri, D. Younesian, Nonlinear harmonic vibration analysis of a plate–cavity system, J. Nonlinear Dyn. 74 (2013) 1267–1279.
[27] M. Sadri, D. Younesian, Nonlinear free vibration analysis of a plate–cavity system, Thin Wall Struct. 74 (2014) 191–200.
[28] F.S. Anvariyeh, M.M. Jalili, A.R. Fotuhi, Nonlinear vibration analysis of a circular plate–cavity system, J. Braz. Soc. Mech. Sci. 41 (2019) 1–13.
[29] M. Amabili, Nonlinear Vibrations and Stability of Shells and Plates, Cambridge University Press, Cambridge, UK, 2008.
[30] M. Amabili, F. Pellicano, M.P. Paidoussis, Nonlinear vibrations of simply supported, circular cylindrical shells, coupled to quiescent fluid, J. Sound Vib. 12 (1998) 883–918.
[31] M. Golzari, A.A. Jafari, Sound transmission loss through triple-walled cylindrical shells with porous layers, J. Acoust. Soc. Am. 143 (2018) 3529–3544.
[32] A.H. Nayfeh, D. Mook, Nonlinear Oscillations, Wiley, New York, USA, 1979.
[33] L.R. Koval, On sound transmission into a thin cylindrical shell under flight conditions, J. Sound Vib. 48 (1976) 256–275.